Received 15 May 2018; | Revised 04 September 2018; | Accepted 00 November 2018

DOI: xxx/xxxx

ARTICLE TYPE

# Micromechanical analysis of sand production

Daniel Garolera[1] | Ignacio Carol[1] | Panos Papanastasiou[2]

[1]Department of Civil and Environmental Engineering, Division of Geotechnical Engineering, BarcelonaTech (UPC), Campus Nord, 08034 Barcelona, Spain
[2]Department of Civil and Environmental Engineering , University of Cyprus, Nicosia, Cyprus

**Correspondence**
Daniel Garolera, Email: daniel.garolera@upc.edu; Ignacio Carol, Email: ignacio.carol@upc.edu; Panos Papanastasiou, Email: panospap@ucy.ac.cy

**Summary**

We present a micromechanical approach based on zero thickness interface elements for modelling advanced localization and cracking states of cemented granular materials, such as reservoir sandstones. The proposed methodology is capable of reproducing the complex behaviour of inter-granular and intra-granular localization, cracking and fracturing of rock formation that leads to sanding in hydrocarbon production. The model is calibrated at the macroscale, using only a few physical parameters, by reproducing the typical behaviour of compression element tests. The model exhibits clear transition behaviour from brittle dilatant to ductile compactant behaviour with increasing confining stress. The methodology is implemented for sand production prediction analysis based on the simulation of 2D micromechanical models of hollow cylinder cross-sections. The obtained results are compared well with published experimental data from hollow cylinder tests characterized by strong scale effect in the range of small perforations.

**KEYWORDS:**
Sand production prediction, sanding, zero-thickness interfaces, micromechanics, localization, cracking

## 1 | INTRODUCTION

The production of sand (also known as sanding) is an unwanted phenomenon that occurs in the production of oil and gas from wells drilled in weakly consolidated formations. Sanding occurs during aggressive drawdowns and it deteriorates with reservoir depletion. According to data from the Society of Petroleum Engineering (SPE), the sanding problem affects nearly 70% of oil and gas wells, as most of these reserves are found in sandy materials[1]. Sanding may cause problems including wellbore collapse, erosion of equipment, cleaning and disposal of produced sand. These problems are more severe in deep-water offshore environment where handling space is limited, safety issues related to hydrocarbon leakage after erosion are critical and intervention for workover is expensive.

Sanding is caused by the increase of the effective stresses sequentially due to a) the stress change in borehole drilling and perforation openings b) the imposed pressure gradient with drawdown and c) the depletion of the reservoir with time. These processes increase the effective stresses near the borehole wall causing damage, fracture and disaggregation of the rock fabric. Damage and disaggregation involves loss of cohesion between grains whereas fracturing may dispatch assembly of grains and isolated areas that are removed and transported by fluid flow, resulting in the production of solid particles. Hence, the factors that influence the production of sand can be classified into three categories related to (i) the geologic formation of reservoirs that may vary from unconsolidated to weakly consolidated (ii) the kind of well completion method such as production from openhole or from cased-perforated wells and (iii) the production strategies, from aggressive production scenarios to water injection for pressure maintenance.

From the engineering point of view, the problem of sand production has been approached with the use of sand avoidance technologies and techniques, called sand control methods. These methods can be classified into: (i) physical exclusion of sand grains with the placement of screen-filters and gravel-packing of the annulus between screens and rock-face and ii) chemical consolidation of formation with resin injection and precipitation of $CaCO_3$. These sand control measures, in addition to their high cost, may block the permeability, stop the production or even fail to control sanding. For this reason, the last two decades, systematic efforts have been made in understanding the mechanisms of sanding in order to model it and improve the recovery techniques[2,3].

Nowadays it is well accepted that certain amount of sand production could be manageable, in order to remove permeability damages due to drilling, enhancing the production. Poor management of this phenomenon can lead to problems of sand over-production with severe consequences. Table 1 shows a list of problems and benefits of not applying sand control. Mathematical models which can predict the critical draw-down and the stage of depletion that will cause sanding are valuable tools for screening the cases that they need sand control. Therefore, the objective is to develop predictive tools for maximizing the production of hydrocarbons while maintaining sand production to acceptable limits.

**TABLE 1** List of pros and cons of no sanding control[2,3].

| Problems | Benefits |
|---|---|
| • Erosion of production equipment. Risk of fire and explosion in gas reservoirs | • Porosity and permeability enhancement. |
| • Well blocking, blockage of tubing assemblage and plugging of the surface facilities. | • Increase oil mobility, due to reduction of resistance to liquid movement. |
| • Increase workover operations to repair or replace equipment and clean wells. | • Foamy oil behaviour, the exosolution and growth of gas bubbles in the soil. |
| • Formation subsidence and casing collapse | |
| • Cleaning of sand impregnated with oil and disposal. | |

The production of sand concerns wells drilled in disaggregatable formations, mainly sandstones but it is also present in calcareous rocks. Due to the wide range of well completion methods, the present work focuses on hydrocarbon production from perforated wellbores in weak formations. For this completion technique, the well is cased and cemented to the formation to isolate and avoid mixing of the different formations fluids e.g. of water with oil or gas, and then is perforated with shape charges (explosives) using downhole perforation guns to communicate the flow from the reservoir into the well (Fig. 1 ). The created perforations are perpendicular to the borehole wall and may vary approximately from 1 cm to 3 cm in diameter and penetrate into rock formation from 20 cm to 50 cm length (see Fig. 1 -left). It is noted that the word 'perforation' refers to small diameter holes embedded in a compressed *insitu* stress field.

From the modelling point of view, a dominant parameter on the load collapse of perforations is the scale effect[4]. Hollow cylinder tests performed on different size holes show that the load required to induce failure is much higher for small holes than for large holes[5,6,7]. Cylinders of small internal diameter consistently break under higher external pressure than cylinders of bigger internal diameter, resulting in failure pressures that may differ more than 3 times. Indeed, the most dominant factor in cylinder strength in the range of perforation size (diameter less than 5 cm) is the scale effect. Because of this strong scale effect, proper modelling of the stability of perforations is a challenging issue.

Considering the small size of the perforation diameter, the formation microstructure plays a significant role. Standard continuum approaches cannot take the microstructure and heterogeneities into account very easily. For example the classical stress analysis (e.g. elastoplasticity) is unable to model the scale effect, since the governing equations can be written in a dimensionless form, predicting for all geometrically similar cylinders the same failure pressure. Earlier attempts to model the localization of deformation and failure of perforations accounting for the scale effect were done using enriched continuum methods such as Cosserat continuum[8,9,10] and gradient plasticity[11,12]. In all these studies no removal of the failed areas and continuation of the

solution after first breakouts were considered. Another continuum approach which is based on fluid-flow, mass balances and erosion mechanisms was developed for weakly consolidated formations [13,14,15,16,17] but those studies were essentially 1D ignoring any changes in the geometry. A physically sound an alternative approach is based on discrete approaches (i.e. DEM). Discrete approaches produce interesting results from a mechanical point of view, as they are able to reproduce the discrete nature of rock and realistic failure kinematics on the basis of conceptually simple and physical model assumptions. However, the main limitation of this approach is the modelling of the fluid flow, which is usually calculated using the FEM on a separate background mesh and then the fluid pressure is "injected" into the DEM model [18,19]. Overall, each of the above techniques has its own drawbacks and limitations related to model calibrations and the size of the real problems.

The present study intends to overcome some of the main drawbacks of existing numerical simulation techniques. A mesoscopic (micromechanical) approach is proposed, in which the grain level is explicitly discretized by using the finite element method with zero-thickness interface elements. The main motivation of the present work is to provide a methodology that can overcome some of those limitations for the modelling of rock sanding production. One objective is to avoid complex theories limited by the kinematics of deformation of continuum media to represent advanced state of failure, mostly due to the propagation of cracks and discontinuities. It is also intended to provide a more satisfactory solution to the flow problem considering the same domain where the open cracks and discontinuities become preferential channels in the flow calculations. For this purpose, a new methodology is proposed based on a mesomechanical approach, successfully used in heterogeneous materials such as concrete [20]. The application of this approach to rock sanding was first proposed in the context of the thesis of Garolera [21,22] in order to obtain a realistic methodology for assessing the risk of sand production and provide a quantitative assessment. In particular, the present study focuses on a 2D analysis of a perforation cross-section (Fig. 1 ).

This paper is structured in 4 main sections. After the introduction to the problem of sanding in this section, we present in Section 2 the application of the microstructure analysis in rock materials that will be used for material characterization. Section 3 is devoted to the methodology of sand production analysis and presents the obtained results of hollow cylinder test simulations. The simulations were made on a prototype material using typical parameters for sandstones. The studies are oriented to model the sensitivity and capability of the method regarding the size effect associated to the hole size and the hole-grain size ratio. The results are compared with published experimental data and other approaches. The main results and conclusions are summarized in Section 4.

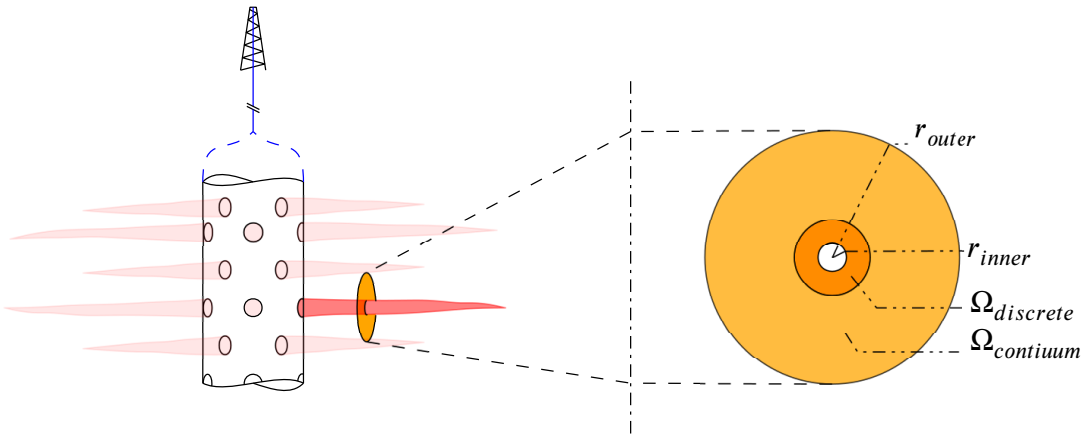


**FIGURE 1** Schematic drawing of a borehole with horizontal drills generated through perforation guns. Study section is presented in orange.

## 2 | MICROSTRUCTURAL ANALYSIS

In this section, a micromechanical approach based on the Finite Element Method with zero-thickness interface elements (FEM+z) is described for the analysis of cemented granular materials, such as sandstones, based on the inter-granular and intra-granular cracking and fracturing. Instead of the phenomenological parameters used in the traditional continuum-based

formulation of the FEM, the proposed methodology is capable of reproducing complex behaviour using only a few physical parameters, though at the expense of discretizing the grain microstructure explicitly. In previous studies this approach has been used successfully to represent the mechanical behaviour of concrete and other quasi-brittle materials under a variety of loading conditions [20,23,24]. The following subsections describe several aspects related to the analysis of the microstructure, with special interest in the generation of material microstructure.

## 2.1 | Microstructural analysis of rock materials.

In the study of physical phenomena, and in particular of mechanics, a key factor is the level of observation. The behaviour observed in experiments is generally complex and attempts to described it with continuum-type models may lead to complex formulations that include non-physical parameters. The homogeneous continuum assumption, traditionally used in engineering studies, may lead to acceptable results at loading levels restricted by the factors of safety. However, in advanced loading stages the material behaviour becomes complex and microstructural consideration becomes essential for reproducing such behaviour, providing a realistic reliable model. Changing the scale of observation and representing explicitly the various material components, such complex behaviour can be reproduced as a result of the overall composite behaviour, even though the behaviour of each individual component is much simpler. For example, in numerical modelling of concrete mechanical behaviour, which has many similarities to rock behaviour, three basic levels of observation were originally proposed by Wittmann [25] (Fig. 2 ):

1. Microscopic level: the internal structure of cement paste and the interfaces between those phases are explicitly represented.
2. Mesoscopic level: the medium is considered heterogeneous, consisting of several phases including the largest heterogeneities (aggregate particles) and a matrix (mortar including smaller aggregates).
3. Macroscopic level: the medium is considered a homogeneous continuum.

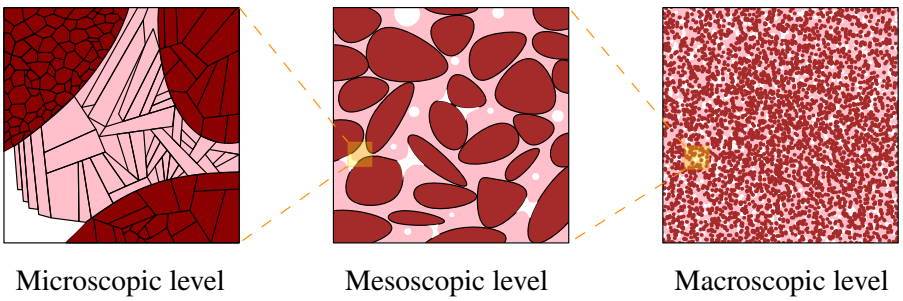


**FIGURE 2** Levels of analysis as proposed by Wittmann [25].

Research experience available in concrete analysis [26,24,23] demonstrates that the intermediate level (mesoscopic level) is adequate to explain most aspects of the observed mechanical behaviour of quasi-brittle materials. This level of analysis allows us to observe the aggregate-matrix interaction, to explain the mechanisms of failure and to model the phenomenon of size effect. Following the proposal of Stankowski [27] followed later by others [28,26], concrete is simulated with two continuum material phases, the aggregates and the matrix, and with two types of interfaces, aggregate-matrix and matrix-matrix. The two continuum phases are discretized with continuum elements (triangles and rectangles, in 2D) and the interfaces with zero-thickness interface elements. An example of a mesh used in the study of crack propagation in concrete is shown in Fig. 3 . Due to the similarity between the observed mechanical behaviour of concrete and rock, the microstructural approach has been applied to the analysis of sandstone rock specimens. Both materials are composed of similar phases, the aggregates correspond to the grains of sand, and the matrix to the cement between particles. Following the common terminology used in the geomechanics literature, this kind of modelling from now in this study will be refereed to as *microstructural modelling*. As mentioned earlier, microstructural analysis has been proven to be especially suitable for the study of materials with quasi-brittle behaviour.

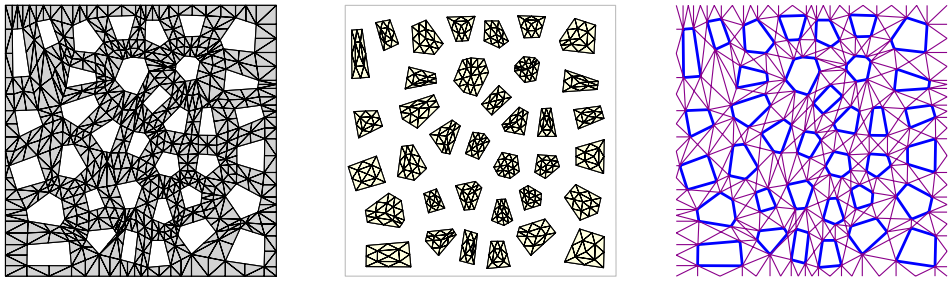

a) Matrix elements b) Aggregate elements c) Interface elements

**FIGURE 3** Microstructural mesh used in the study of crack propagation in concrete proposed by Lopez[26] a) discretization of matrix; b) discretization of aggregates; and c) interface elements.

A qualitative representation of quasi-brittle behaviour is depicted in Fig. 4 , where the average stress-strain curve of an ideal uniaxial tensile test is presented. The beginning of the curve is characterized by an elastic behaviour (up to point A), followed by a loss of elasticity due to micro-cracking emanating before reaching the peak (point B). The peak strength occurs when micro-cracks coalescence into a macro-crack. After reaching the peak, the coalescence of micro-cracks into macro-cracks continues (point C) until reaching a residual state (D) where tensile or cohesion strength is lost and the blocs continue sliding with friction.

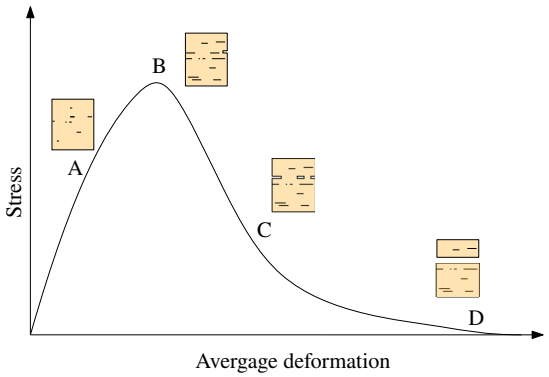


**FIGURE 4** Schematic of a average stress-strain curve with softening for a quasi-brittle material.

Due to the small grain size, average diameter between 0.1 mm to 1.0 mm, for the applications to rock, the original microstructural geometry of Fig. 3 has been simplified in order to reduce the number of elements and nodes. For this reason, the continuum elements belonging to the matrix phase have been replaced by an appropriate contact behaviour between grains, which includes the behaviour of the matrix phase (see Fig. 5 ). This simplification may be reviewed in future studies, depending on the available computational resources. The microstructural study used in this study uses a combined procedure. The rock behaviour is represented by a continuum medium containing a grid of zero-thickness interface elements. This formulation due to the displacement and stress jumps provided by the interfaces allows for localization of the deformations as approaching material failure.

One of the main advantages of this type of modelling is the intrinsic incorporation of two characteristic lengths. One related to the grain size and the other due to the use of relative displacements and the constitutive law that include fracture energy parameters $G_f^I$ and $G_f^{IIa}$ for the mechanical formulation of the interfaces. The introduction of an energetic criterion for failure as compared to more traditional strength criterion automatically generates a size effect in the results with subsequent characteristic length[29,4].

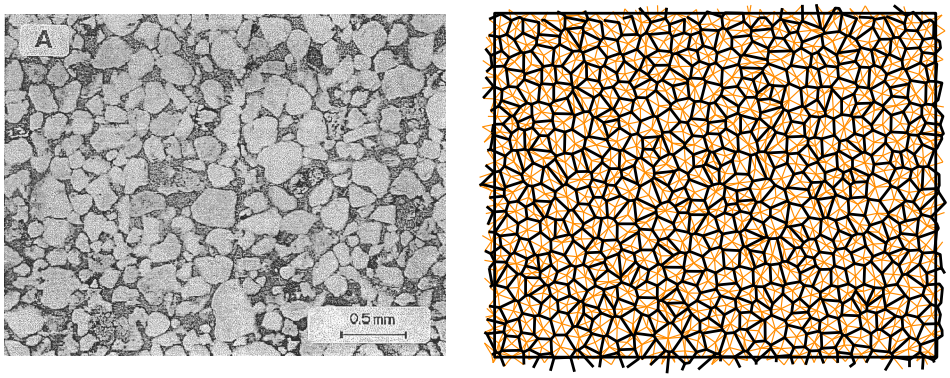


a) Real rock microstructure b) Idealized microstruture

**FIGURE 5** Comparison between a real sample: a) Micro-photograph from a sandstone sample and b) the interface layout of idealized model with FEM+z. In dark, contacts between grains and, in pale, intra-granular cracks.

## 2.2 | Microstructure generator

An important aspect of the work described in this study is the generation of micro-geometries and the corresponding FE meshes. Efforts have been aimed at obtaining an automatic mesh generation procedure with the following requirements: 1. Grains of approximately equal size distributed randomly. 2. Intergranular phases idealized as contacts between grains.

The process can be summarized in the following steps (see Fig. 6 ): 1. Generation of a initial grid of points with random distribution. 2. A network of triangles is generated using a *Delaunay* triangulation, where the vertices are the random points generated in step 1. 3. A *Voronoi* tessellation is obtained from the *Delaunay* triangulation of step 2. At this point, a filter is introduced to remove the small sides and therefore avoid elements with poor geometric ratios. 4. Discretization of polygons in triangular elements and introduction of interface elements of zero thickness between continuum elements.

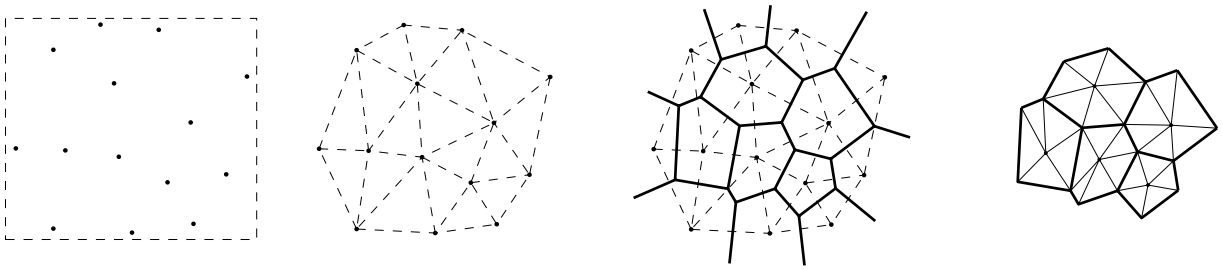

a) Grid of points b) Delanuay triangulation c) Voronoi tessellation d) Element discretization

**FIGURE 6** *Delaunay-Voronoi* based mesh generation method: a) random node distribution, Delaunay vertices, b) *Delaunay*'s triangulation, c) *Voronoi* tessellation, and d) element discretization, black thicker lines correspond to the inter-granular zero-thickness interfaces, and orange thiner lines to intra-granular zero-thickness interfaces.

## 2.3 | Mechanical constitutive law for interfaces

One of the fundamental points of any mechanical modelling is the constitutive law, the relationship between deformations and stress. In the particular case of zero-thickness interface elements this relationship is established between the relative displacements ($\mathbf{r}$), which take a role analogous to strain in continuum elements, and the conjugate measure, the stress tractions on the interface plane ($\boldsymbol{\sigma}_{\text{J}}$). Both variables are evaluated at the mid-plane of the interface using a local reference system. The material behaviour is formulated in terms of normal and tangential components of stress and relative displacements on the interface plane.

In this study two constitutive laws for interfaces are used, a basic elastic relationship and a fractured-based elasto-plastic law. The elastic law is defined by means of two parameters, the normal ($K_n$) and tangential ($K_t$) stiffness coefficients. With these definitions, the elastic stiffness matrix ($\mathbf{D}_j^{el}$) becomes diagonal:

$$\boldsymbol{\sigma}_j = \mathbf{D}_j^{el}\mathbf{r} \Rightarrow \begin{pmatrix}\sigma_n\\ \tau\end{pmatrix} = \begin{pmatrix}K_n & 0\\ 0 & K_t\end{pmatrix}\begin{pmatrix}r_n\\ r_l\end{pmatrix} \tag{1}$$

In general, the values given to elastic coefficients ($K_n$, $K_t$), may be fixed in two ways: (a) if the interface represents a potential fracture line with no intrinsic elastic deformability, they may be considered as penalty coefficients and be assigned very high values compatible with numerical well-posedness; (b) if the interface represents some thickness of deformable material, or a weak material interface with intrinsic deformability, $K_n$ and $K_t$ can be assigned with the corresponding physical values. In the subsequent examples analysed we use the second case.

The fracture-based constitutive equation is expressed by an elasto-plastic law in which the state variable is formulated in terms of energy [30,26,31]. The model, based on the theory of elasto-plasticity, includes concepts of fracture mechanics and fracture energy parameters. For this model, a three-parameter hyperbolic fracture surface [30] has been adopted:

$$F(\boldsymbol{\sigma}_j, W^{cr}) = |\tau|^2 - (C - \sigma\tan\phi)^2 + (C - \chi\tan\phi)^2 \tag{2}$$

where $\tau$ is the shear stress, $\sigma_n$ is the normal stress, $\chi$ is the vertex of the hyperbola representing the tensile strength, $C$ is the cohesion obtained as $C = (a+\chi)\tan\phi$, $\tan\phi$ is the friction angle and $a$ is the distance to the tip of the hyperbola to the asymptote apex as shown in Fig. 7 . The parameters that control the two fracture modes described above are the classical fracture energy in Mode I, $G_f^I$ (pure tension), and the additional Mode IIa fracture energy, $G_f^{IIa}$ (shear-compression).

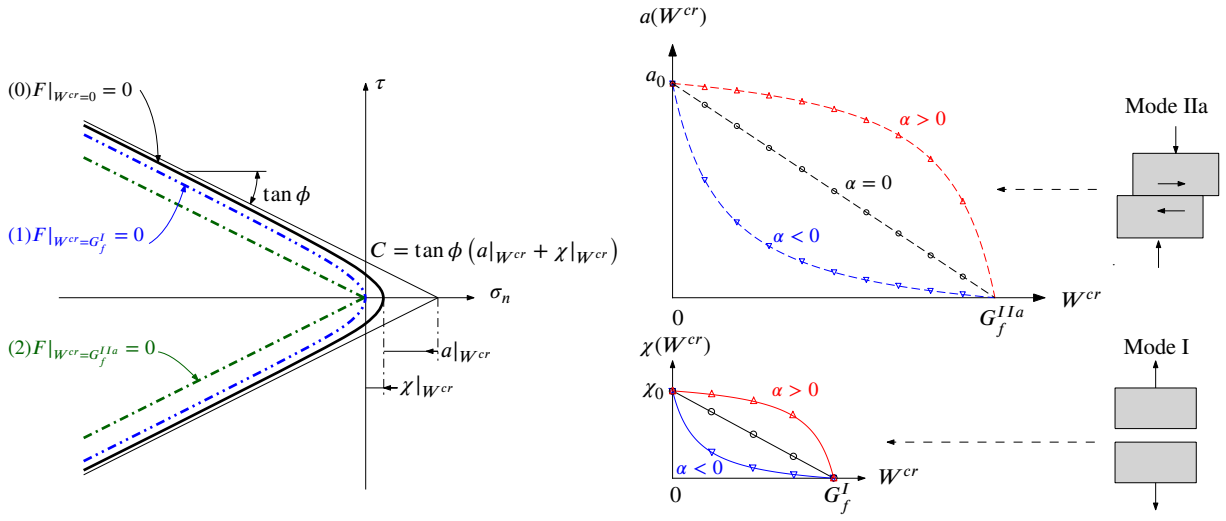


**FIGURE 7** Constitutive model of the interface: fracture surface(left), and basic modes of fracture development with softening laws (right).

The evolution of the fracture surface has three steps. Once the crack has started opening, the fracture surface starts contracting and the stresses starts decreasing, so that the updated stress point always remains on the surface. For a given initial fracture surface, represented by curve "0" in Fig. 7 left, its final configuration will depend on the specific mode of fracture taking place. For pure tension (Mode I) a fully developed crack requires that normal separation of the two sides of the interface be allowed, as the only kinematic condition. Because of the material's heterogeneity the cracking surface is rough and the final fracture surface is a hyperbola with vertex at the origin, given by curve "1" in Fig. 7 left. The other limit situation corresponds to cracking under shear and very high compression with no dilatancy, which is called "asymptotic mixed mode" or Mode IIa [32]. In this second fracture mode, slip occurs in the tangential direction with no normal dilatancy allowed, and the final fracture surface is defined by a pair of straight lines representing pure frictional behaviour (curve "2" in Fig. 7 left).

## 2.4 | Micromechanical testing

The capabilities of the described model are demonstrated by simulating a biaxial experiment on a weak sandstone. Modelling of the biaxial test is a standard simulation used in the literature in order to validate computations on localization of deformation and advanced failure states. The biaxial test can demonstrate clearly the shearband patterns and their orientation. The theory will be used in the next section to analyse the more complex problem of sanding.

The domain that is considered is in 2D and consists of a square specimen with approximately 40x40 grains. The values of the specimen dimensions ($l_0$) and grain size ($\varnothing_{grain}$) used in the examples, are specified in Fig. 8 . In order to include the possibility of intra-granular cracking, zero-thickness interface elements have been inserted, not only along the inter-granular boundaries, but also across grains, as already described in Section 2.2.

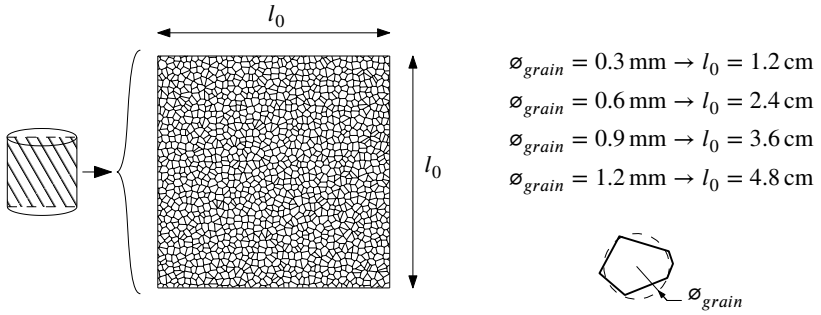


**FIGURE 8** Model geometry of the biaxial compression test considering rock microstructure.

The geometry and the applied boundary conditions of the biaxial compression test (BCT) are shown in Fig. 9 . A hydrostatic uniform stress state of value $\sigma_0$ is applied first followed by a deviatoric load applied incrementally by prescribing the vertical displacement on the upper side of the specimen. Due to the expected softening behaviour, an arc-length method was employed in the numerical analysis in order to control the post-peak response. No imperfection is needed to trigger localization.

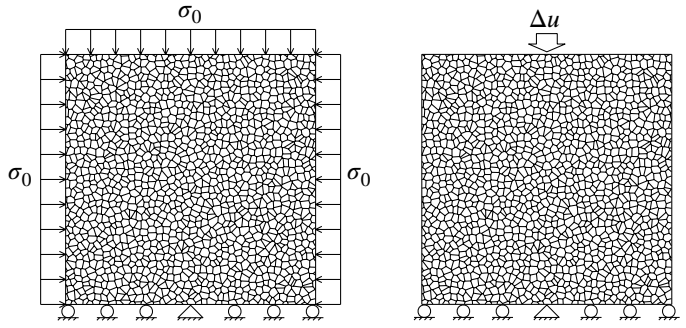


**FIGURE 9** Boundary conditions of the BCT: left) Confining step and right) deviatoric step.

### Material properties

The micromechanical testing has been performed using an academic example based on typical parameter values of the *Red Wildmoor* sandstone[33]. The parameters used by the model are presented in Tables 2 and 3 . Table 2 shows the material parameters that define the continuum behaviour, which have been assumed equal to the typical values of quartz grains. Table 3 , lists the parameter values of the interface. The elastic stiffness coefficients $K_n, K_t$ had been fixed so that the overall elastic behaviour of the sample matches the *Red Wildmoor* elastic modulus of approximately 14.0 GPa (which is lower than the 34.0 GPa

of quartz grains). This aspect is discussed later in more detail with a sensitivity study. The initial values of fracture surface parameters $\chi_0$, $C_0$, and $\tan\phi$ determine the overall peak strength of the sample, and the fracture energy parameters $G_f^I$ and $G_f^{IIa}$ are responsible of how fast the stress decays after the peak. A trial and error procedure has led to the values for all those parameters shown in Table 3 . Note that the values of $G_f^I$ are in the range of experimental values[34], while $G_f^{IIa}$ is normally given values one to two orders of magnitude higher[30]. Finally, the value of $\sigma_{dil}$ determines the normal stress level for which any shear dilatancy is suppressed at the interface level, and therefore also is substantially reduced at the overall triaxial level. In the absence of detailed information the value assumed for this parameter is in the order of the overall UCS.

**TABLE 2** Material properties of continuum phase.

| *Parameter* | | *Value* | *Units* |
|---|---|---|---|
| E | Young's modulus | 34.0 | GPa |
| $\nu$ | Poisson's ratio | 0.27 | - |

**TABLE 3** Material properties of interfaces.

| *Parameter* | | *Value* | | *Units* |
|---|---|---|---|---|
| | | Inter-Grain | Intra-Grain | |
| $K_n$ | Normal stiffness | $10^5$ | $10^5$ | $\text{GPa} \cdot \text{m}^{-1}$ |
| $K_t$ | Tangential stiffness | $10^5$ | $10^5$ | $\text{GPa} \cdot \text{m}^{-1}$ |
| $\chi_0$ | Tensile strength | 0.4 | 0.8 | MPa |
| $\tan(\phi)$ | Friction angle | 0.5773 (30.0°) | 0.5773 (30.0°) | |
| $C_0$ | Cohesion | 4.0 | 8.0 | MPa |
| $G_f^I$ | Energy mode I | $0.006 \cdot 10^{-3}$ | $0.026 \cdot 10^{-3}$ | MPa · m |
| $G_f^{IIa}$ | Energy mode IIa | $0.1 \cdot 10^{-3}$ | $0.4 \cdot 10^{-3}$ | MPa · m |
| $\sigma_{dil}$ | Sigma dilatation | 10.0 | 10.0 | MPa |

## Results

The numerical simulations have been performed using the research group's FE code DRAC[35]. The first analysis is conducted for a fixed grain size of 0.6 mm with double value of strength parameters of intra-grain with respect to inter-grain interfaces. After reaching the peak stress, the deformation starts localizing and the stress-strain curve follows a softening branch. The evolution of crack propagation for the case of 1 MPa confinement is presented in Fig. 10 . Each picture shows progressively the deformation pattern which corresponds to the post-peak loading stages marked as points A, B, C, etc. on the stress-strain curve (top). The resulting stress-strain curve exhibits a smooth transition in the softening regime which leads to progressive localization. One can clearly identify the qualitative patterns of localization and fracture propagation described above: micro-cracking, coalescence into macro-cracks, and localized state. The angle between the direction of the minimum applied stress (horizontal) and the crack pattern turns out to be $60^o$ which is in a good agreement with the expected theoretical value of $\beta = 45 + \phi/2$. This inclination is clearly different from any mesh directionality which does not exist. In other words, the results do not depend on the orientation of the mesh as in the case of computations based on a classical continuum

Figure 11 shows the biaxial strain-stress curves obtained for different values of the confining stress: 0 MPa, 1 MPa, 5 MPa, 10 MPa, 20 MPa and 40 MPa. The results obtained show increasing strength characterized by transition from brittle to ductile behaviour with increasing confinement. Figure 12 shows the volume changes with shearing. The results show clearly that the behaviour starts with specimen compaction and then dilates with advancing shearing. As expected, the increase in the confining pressure delays the transition from compaction to dilation. Figure 13 represents the crack pattern obtained at the end of each simulation with different confining pressures. As this results correspond to different loading levels no direct comparison can be

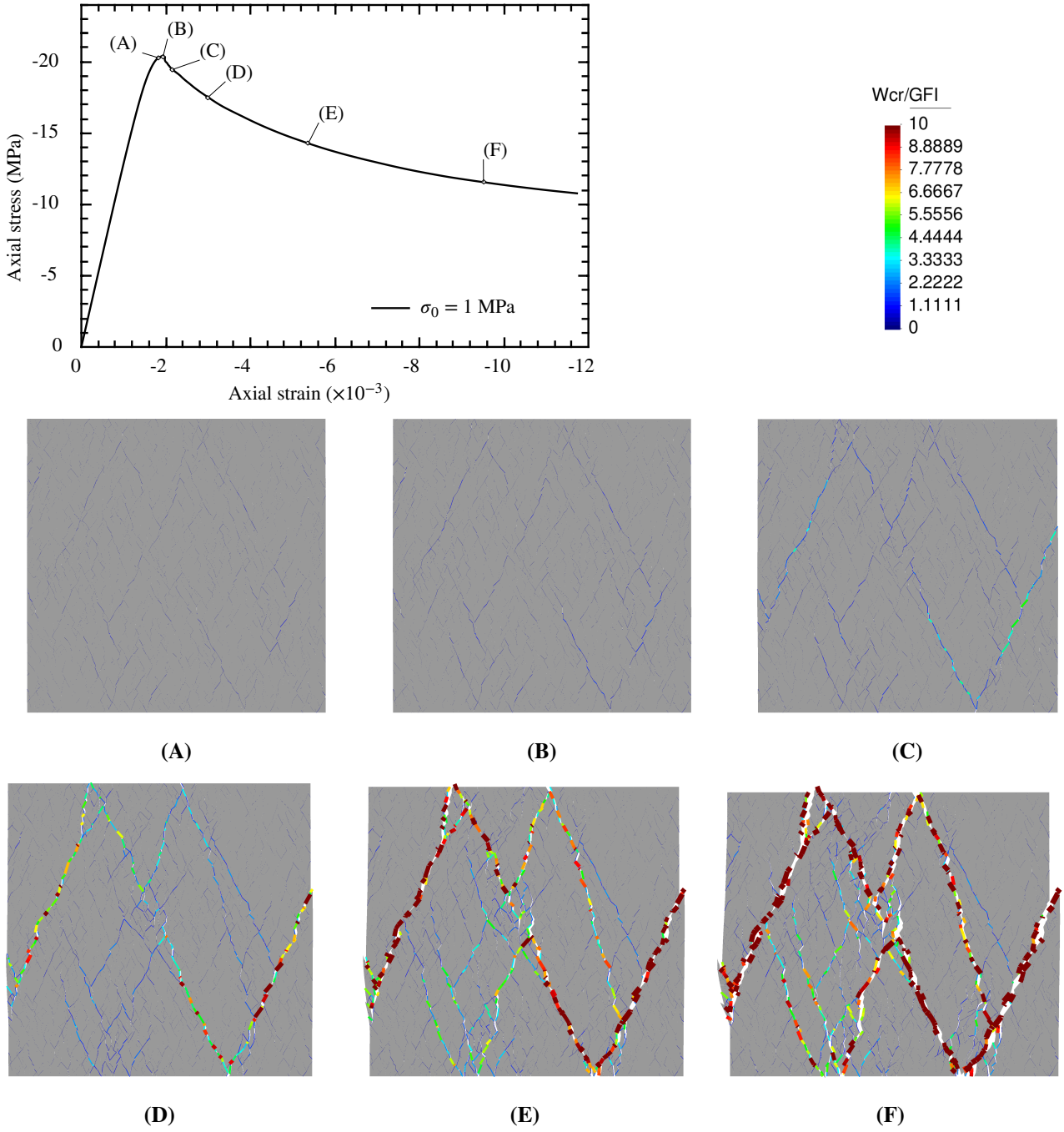


**FIGURE 10** Evolution of fracture propagation for 1 MPa confinement: average stress-strain curve obtained for biaxial compression in 2D (top) and normalized energy spent along interfaces ($W^{cr}/G_f^I$). Results were plotted on the deformed mesh (magnification ×5) (bottom, A-F).

made. Nevertheless, it is clearly observed that, as the confinement increases localization is less pronounced. In conclusion, the results show that this approach is capable of representing brittle-ductile transition without introducing additional ingredients.

The sensitivity to microstructure is examined next by considering the effects of intra-granular strength and grain size. Figure 14 shows the average stress-strain curves obtained for three cases of intra-granular strength: a) infinite value, b) double inter-granular strength and c) same as the inter-granular strength. It can be observed that intra-granular strength values influence dramatically the resulting behaviour of the overall material. By not allowing intra-granular cracking leads to an upper bound of the mechanical behaviour for which failure under uniaxial compression is not reached during our calculations. On the other

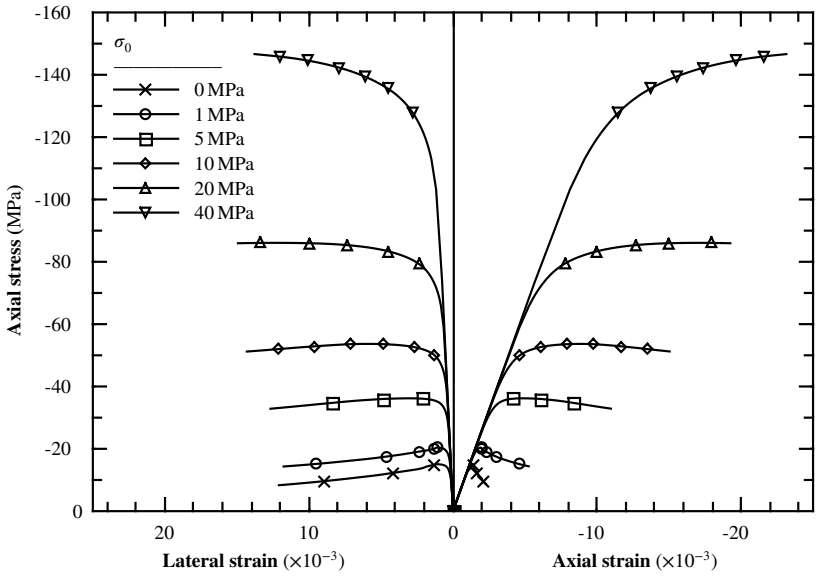


**FIGURE 11** Stress-strain curves for different levels of confinement.

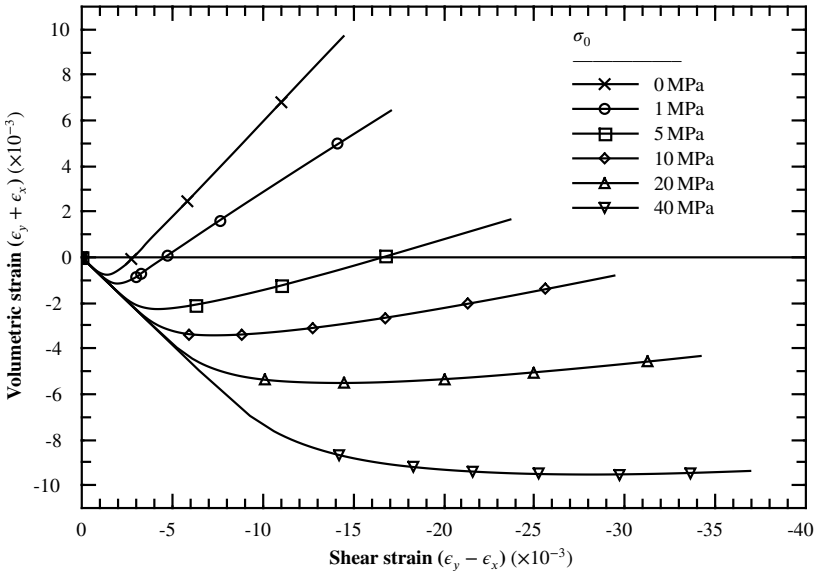


**FIGURE 12** Volumetric vs shear strain curves for different levels of confinement.

end, the case c) approaches the behaviour of a quasi-brittle material without the granular structure considered (since cracks can develop equally through and between grains). This case leads to a lower bound of the overall strength. Finally, option b) with the right choice of parameters represents a more realistic intermediate case. The material post-peak response is also influenced by the grain strength (Fig. 14 ). The overall model behaviour becomes more brittle as the intra-grain resistance increases.

Fig. 15 depicts the general crack pattern obtained with some enlarged details of a section of a main macro-crack for the three assumptions of intra-granular strength. For the case b) with double strength, the cracks are opening and sliding around grains except at certain very specific points where grains crack due to high stress concentration. In case c) grain cracking happens systematically where this does not happen at all in case a). These details of micromechanical cracking may assist understanding the resulting overall stress-strain curves of Fig. 14 . A first conclusion from these results is that the direct uniaxial compression test is very sensitive to grain strength, and that some form of intra-granular cracking must be allowed for a realistic description of the direct uniaxial compression test of a granular material using Voronoi-generated grain geometry.

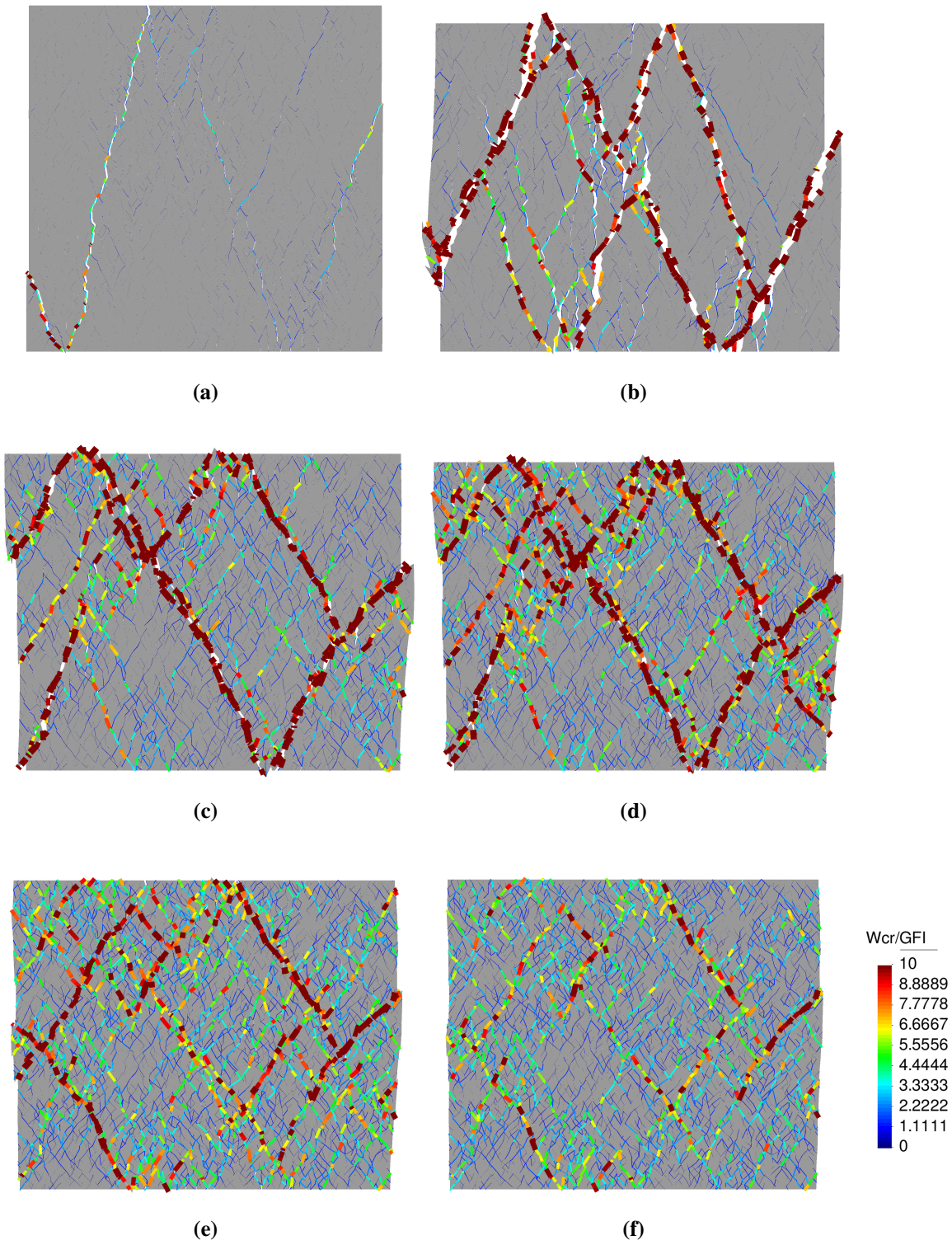


**FIGURE 13** Results of the 2D "triaxial" compression test at various confinement pressures. Normalized energy spent ($W^{cr}/G_f^I$) at: a) No confinement; b) 1 MPa; c) 5 MPa; d) 10 MPa; e) 20 MPa; and f) 40 MPa. Results plotted on the deformed mesh (magnification ×5) for the final state reached in each simulation.

The effect of grain size is analysed using the size values shown in Fig. 8 , $\varnothing_{grain}$ = 0.3 mm, 0.6 mm, 0.9 mm and 1.2 mm. For this purpose, the coordinates of the original mesh are transformed (scaled) to obtain a mesh with the desired grain size. The

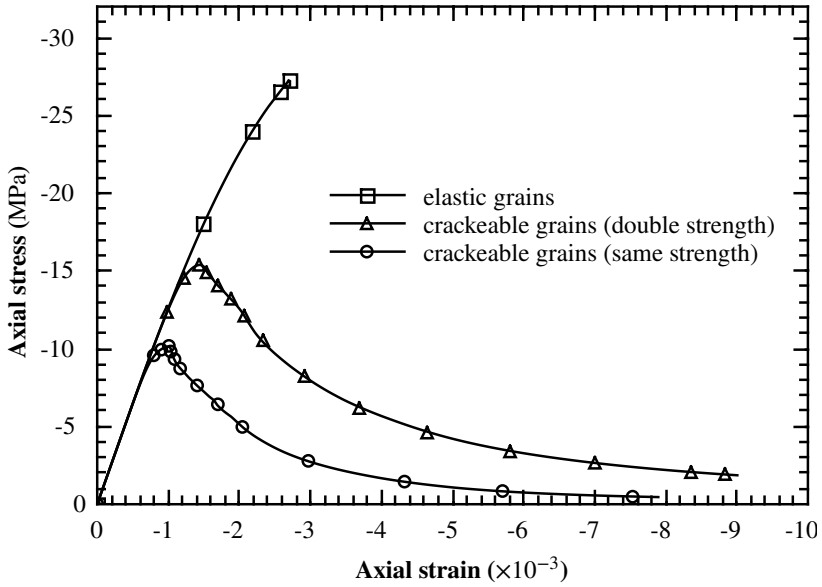


**FIGURE 14** Average stress-strain curves for the uniaxial compression simulations, with three different assumptions for intra-granular cracking: 1) grains are elastic and do not crack, 2) strength parameters are double than those of inter-granular fractures and grains can crack, and 3) grains can crack, and strength is the same and grains can crack.

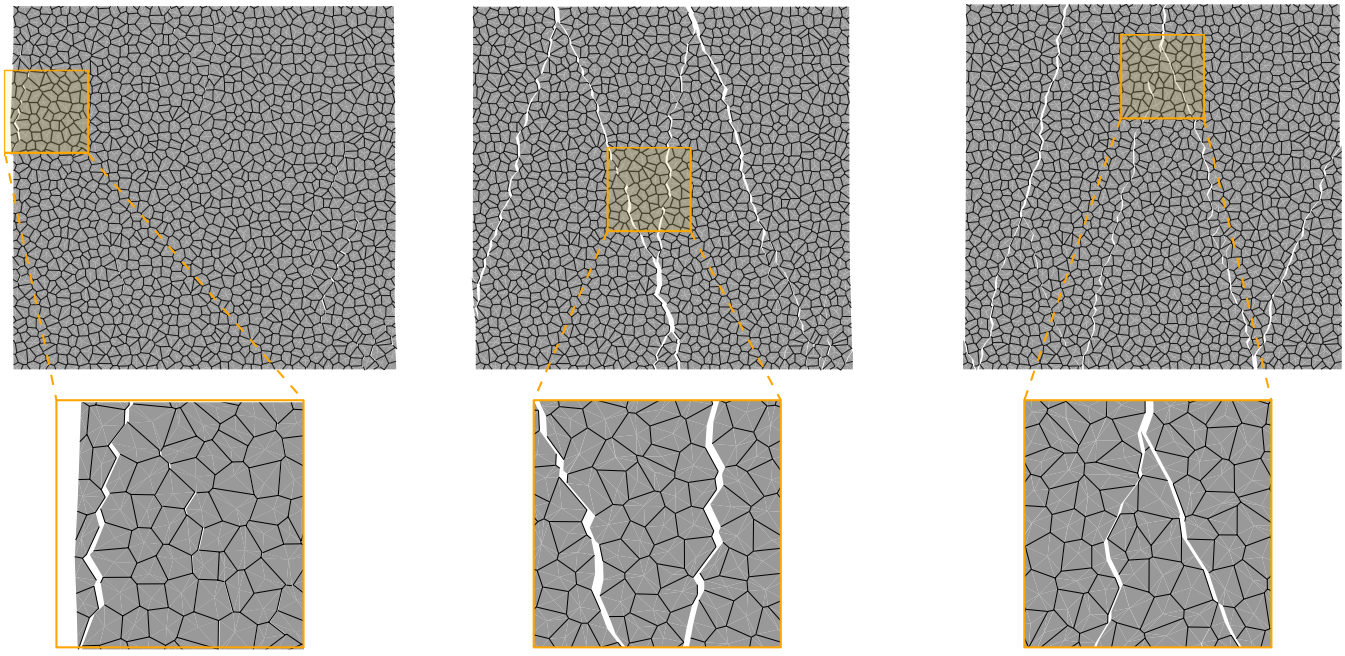

a) Elastic grains (Deformation ×10)

b) Crackeable grains (double strength) (Deformation ×1)

c) Crackeable grains (same strength) (Deformation ×2)

**FIGURE 15** Mesh deformations for UCT at different values of grain resistance: a) elastic grains; b) fracture grains (double resistance) and c) fracture grains (single resistance).

material parameters remain the same as in the previous example (Tables 2 and 3 ) and the boundary conditions similar to the unconfined compression test analysis.

Figure 16 shows the resulting stress-strain curves at the macroscopic level for the different grain sizes. It is clear that the peak stress of the sample does not depend on the grain size. It is also observed that the initial elastic stiffness of the overall system, decreases with decreasing grain size. This decrease is explained by the reduction in the number of interfaces per unit thickness of material with decreasing grain size. Assuming, as a first approximation, that the equivalent stiffness of the system ($E_{eq}$) may be represented as a series arrangement of continuum and interfaces, the overall equivalent elastic modulus of the overall system would be expressed as:

$$\frac{1}{E_{eq}} = \frac{1}{E} + \frac{n}{K_n} \tag{3}$$

where $n$ is the number of interfaces per unit length. The increase of the number of interfaces per meter (when $\varnothing_{grain}$ is reduced) leads to lower elastic modulus and to "dilution" of Poisson's ratio. The values of Table 4 compare well with the analytical solution provided by Eq. (3) in the case of $K_n = 10^5\,\mathrm{GPa}\cdot\mathrm{m}^{-1}$. Note that as the number of interfaces per unit thickness is increased the above expression predicts that the equivalent elastic modulus decreases, as observed in the FE calculations depicted in Fig. 16 .

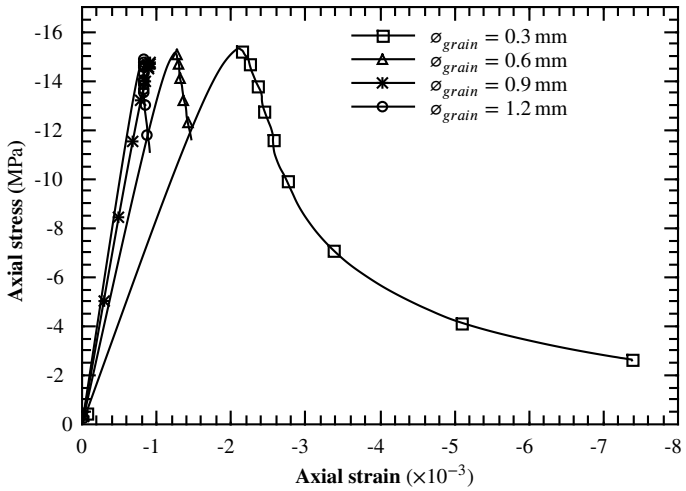


**FIGURE 16** Stress-strain curves for uniaxial compression test with different average grain size.

Figure 17 shows the value of $E_{eq}$ as a function of the grain size for different values of the interface stiffness coefficient. The results are obtained with the analytical expression (3) assuming that the number of interfaces per unit length is given by

$$n = 3\left(\frac{1}{\varnothing_{grain}}\right) \tag{4}$$

where $\varnothing_{grain}$ is in m. The curves of Fig. 17 indicate that, if one wants the overall stiffness to approach the grain stiffness, for the range of grain sizes considered, it would require interface stiffness of the order of $10^7\,\mathrm{GPa}\cdot\mathrm{m}^{-1}$ or more, which means at least two orders of magnitude higher than the value considered ($10^5\,\mathrm{GPa}\cdot\mathrm{m}^{-1}$). The convenience of such condition has to do with the discussion whether the interface stiffness has the physical meaning of the stiffness of the cementing materials or it is rather considered a numerical artefact (penalty coefficient) as already explained in Section 2.3.

**TABLE 4** Equivalent parameters from micromechanical analysis.

| *Parameter* | | $\varnothing_{grain}$ | | | | *Units* |
|---|---|---|---|---|---|---|
| | | 0.3 | 0.6 | 0.9 | 1.2 | mm |
| E | Young's modulus | 7.77 | 13.66 | 17.25 | 19.8 | GPa |
| $\nu$ | Poisson's ratio | 0.14 | 0.15 | 0.18 | 0.21 | - |

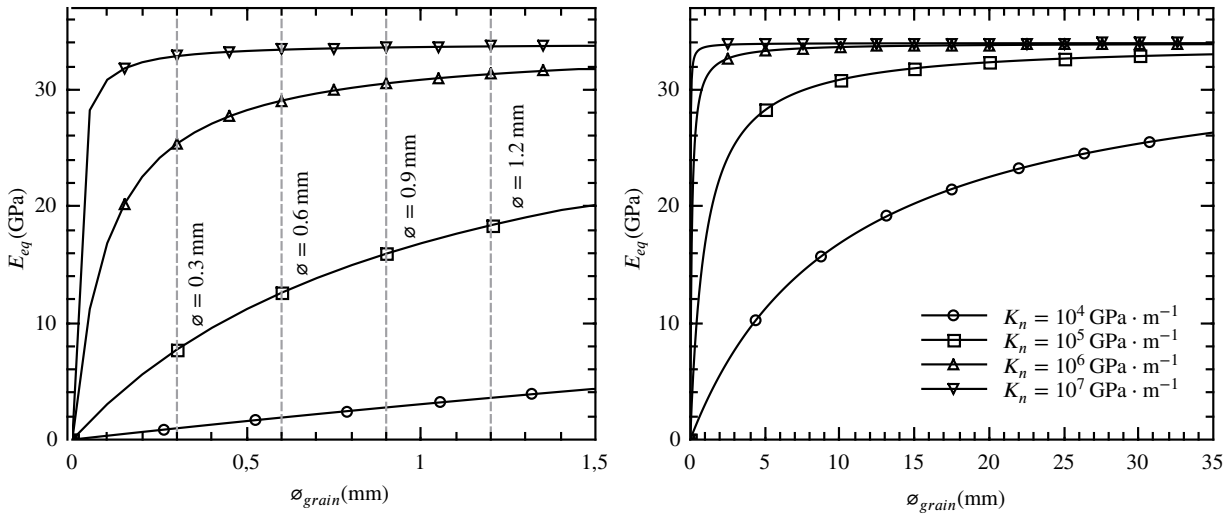


**FIGURE 17** Equivalent elastic modulus for different grain sizes and interface stiffnesses.

## 3 | METHODOLOGY OF SAND PRODUCTION ANALYSIS

The methodology which has been implemented for sand production analysis is based on the simulation of 2D micromechanical models of hollow cylinder cross-sections. This section describes the main aspects related to model generation and numerical techniques used for such analysis.

The methodology implemented is based on the assumptions explained hereafter. The calculation is performed with small deformation theory and carried out in 2D. It is assumed here that the deformation of the thick walled cylinder under external loading is the same in every cross-section perpendicular to the borehole-axis and the out of plane deformation (parallel to the borehole axis) can be neglected. Therefore a 2D analysis can be carried out in one such plane cross-section with plane strain conditions. Cracks which totally open in between and inside grains are identified and an automatic criterion detects the cases in which the crack trajectory is closed, isolating a grain or group of grains. The effects of the axial fluid-flow are not explicitly taken into account since the study is a two-dimensional. However, it is indirectly considered that the elimination of the detached grains or groups of grains is the result of this agent. Although formation damage is present due to the perforating procedure [36], this effect is not considered in the initial simulations as cleaning procedure may remove the damaged area before normal production. Due to the discretization area, the cracking and detachment of grains will only be observable in the vicinity of the perforation (discrete domain) as expected. Finally, due to computational limitations, the minimum grain size considered in this analysis is 0.6 mm.

As already mentioned, the simulation of sand production is based on the analysis of 2D cross-sections. In order to reduce the number of discretized elements, the model is split into two subdomains: an inner discrete domain around the perforation hole, in which the microstructure is explicitly represented and an outer continuum domain extending to a sufficiently large distance to eliminate any boundary effects.

The generation of the above geometric sand models is carried out into three consecutive steps:

1. **Generation of the discrete domain**. The initial microstructural mesh is generated using the *Delaunay-Voronoi* procedure for an initial square domain (Fig. 18 a) from which all elements, the baricenter of which fall inside the specified inner radius ($r_{inner}$) or outside the outer radius ($r_{outer}^{discr}$) are removed. In this way, a domain in the form of a circular ring is obtained (Fig. 18 b) with non-smooth inner and outer surfaces following the triangle edges. In the cases analysed, the ring thickness is taken as approximately equal with the perforation diameter and a minimum thickness of 10 grains in order to ensure that the relevant normal and shear stress gradients are located in the inner discrete domain near the hole. The radius of the boundary between the discrete and continuum domain was approximately defined in this study, to be at least two times the internal radius of the hole as the stress concentration and the damage around a pressurized cavity is mainly restricted to a distance from the hole wall of approximately one radius [5,6,7,8]. The validity of this assumption was confirmed posteriori by the computational results.

2. **Generation of continuum domain**. In order to ensure that the remote boundary conditions are correctly represented, the mesh is extended with conventional continuum elements to the limit of the domain (Fig. 18 c-d). Hence, the outer domain is defined between the inner radius ($r_{inner}^{cont}$), which is the same as the outer radius of the discrete domain ($r_{outer}^{discre}$), and the outer radius ($r_{outer}$) where the remote boundary conditions will be applied. In order to ensure the perfect match between the meshes of the inner and outer domains, first the polyline constituting the outer boundary of the inner ring is precisely identified and then used as boundary of the domain to be meshed with continuum elements.

3. **Domain assembly and generation of input data**. The final mesh consists of the union of both inner and outer domains. In order to join the meshes, first the common nodes are detected and then the nodes and elements of the outer mesh are renumbered. Additionally, a perimeter set of joints is generated along the boundary between the inner and outer domains as the zero-thickness interface elements from the inner domain have to end in "T"-type intersections with other interface elements (and can not simply end in the middle of the continuum mesh). Since in this study interface elements are deformable (stiffness is not a penalty coefficient with very high value), the non-smooth shape of the perimetral contact may certainly generate stress fluctuations, specially in the case of sharp angles. However these would be only local fluctuations around the contact line, which will not generate any cracking or sliding because of the elastic behaviour assumed for this contact. Average stress values on both sides of the contact should be the same due to the imposed equivalence of average elastic parameters (Table 4 ). In any case, to minimize the possible elastic fluctuations, the sharpest angles of the boundary have been identified and manually modified before generating the outer domain. During this stage a number of utility files for later post-processing stresses, etc. are also generated. Figure 18 e-f shows some details of one of the discretizations performed.

## 3.1 | Solid Production simulation

One of the most sensitive developments in the sand production modelling is the grain extraction criterion. The methodology implemented for this purpose was based on (i) definition of the crack failure criterion (zero-thickness interface element failure), and (ii) definition of a criterion for removing a grain or set of grains.

The criterion of crack failure was developed using the internal variable of the interface constitutive model which consists of the energy dissipated in fracture process ($W^{cr}$). This energy normalized with respect to strain energy release rate $G_f^I$ is compared to a threshold value, typically fixed to 0.7, which is indicative of severe tensile degradation of the interface. Note that for an interface element to be marked as totally cracked, the following condition must be fulfilled at its all Gauss points,

$$\frac{W^{cr}}{G_f^I} \geq 0.7 \quad \Rightarrow \quad failure \tag{5}$$

Once the cracked interfaces are identified, a criterion for grain extraction is utilized. This procedure consists of removing the grains or groups of grains that are isolated from the medium by the fractured interface elements that start and end at the free surface of the inner perforation. The procedure has been automated with the inclusion of a module in the DRAC code[35] that checks the cracking and extraction criteria at the end of each incremental step.

Figure 19 summarizes the different steps involved in the sanding algorithm:

1. **Tree algorithm** over cracked interfaces. This algorithm looks for any path of cracked interfaces that isolates a part of the discrete domain from the rest of the domain. First, the interfaces with nodes on the inner perforation boundary are checked to detect if they are cracked. Once this criterion is satisfied, a tree algorithm is used to check for any path of cracked fractures that leads to another node of the inner surface, different from the initial one (Fig. 19 b). In the case of finding a fracture that isolates a part of the domain, then an algorithm is activated to detect the grains to be eliminated. If several paths are found with one inside the other, the algorithm selects the maximum envelope.

2. **Elimination of grains**. In case that any crack path exists that isolates a grain or group of grains, the removal algorithm is started (Fig. 19 c). This automatic algorithm is based on the excavation procedure already existing in DRAC which can be divided in two steps:

   (i) Evaluation of excavation forces ($F_{exc}$). The excavation forces are computed using the appropriate integral of stress over the removed (excavated) domain ($\Omega_r$) (Eq. (6)). The computation of equivalent nodal forces ($F_{exc}$) due to excavation is only applied to existing nodes. Due to the fact that from the viewpoint of flow the excavation procedure

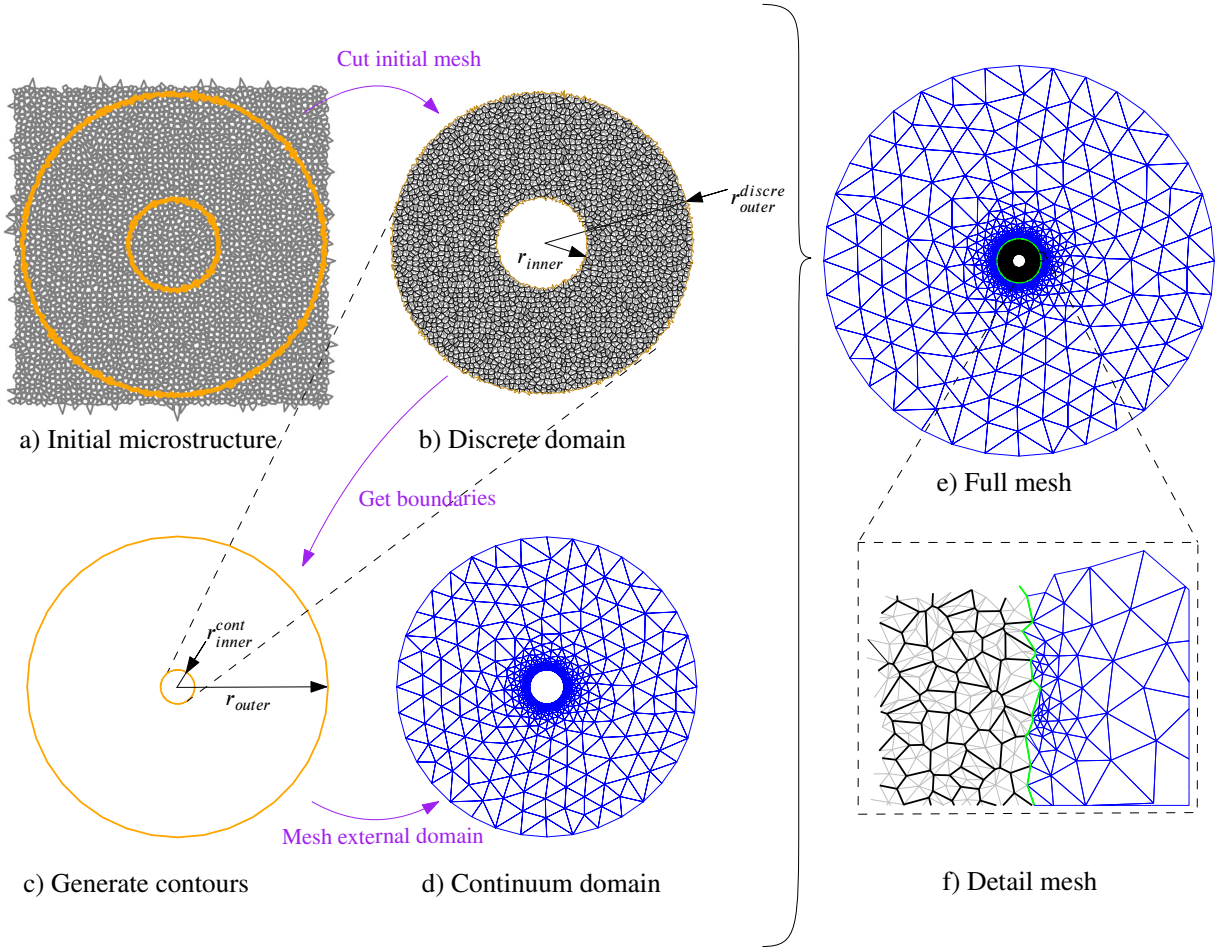


**FIGURE 18** Generation of the sand production geometry model: a) initial mesh generated via Delaunay-Voronoi b) ring-type inner domain c) geometry of the outer perimeter d) continuum outer domain e) complete mesh and f) detailed view of the inner domain, showing mesh distribution of grains.

takes place in steady state conditions, the evaluation of internal forces can be carried out directly in terms of the effective stress.

$$F_{exc} = \int_{\Omega_r} B^{\top} \boldsymbol{\sigma}' \, d\Omega \tag{6}$$

(ii) Application of excavation forces. The excavation forces are assembled into the load vector (or right hand side vector) and are applied in small increments.

3. **Generation of data files** for the subsequent calculations. These are the files indicating which elements have to be removed in the excavation process, and what forces have to be applied on the remaining nodes.

In order to improve the performance of the procedure, a hierarchical model of the mesh geometry including grains and interfaces is generated at the beginning of the calculation, which contains the list of connectivities of joints and grains.

## 4 | HOLLOW CYLINDER TEST (HCT) MODELLING

One of the most common laboratory tests to evaluate and quantify the risk of sand production in real rock samples is the Hollow Cylinder Test (HCT). Therefore, it seems a logical step to verify the proposing numerical model for sand production and to calibrate its parameters using experimental results of HCT test. This section describes the application of the proposed model for

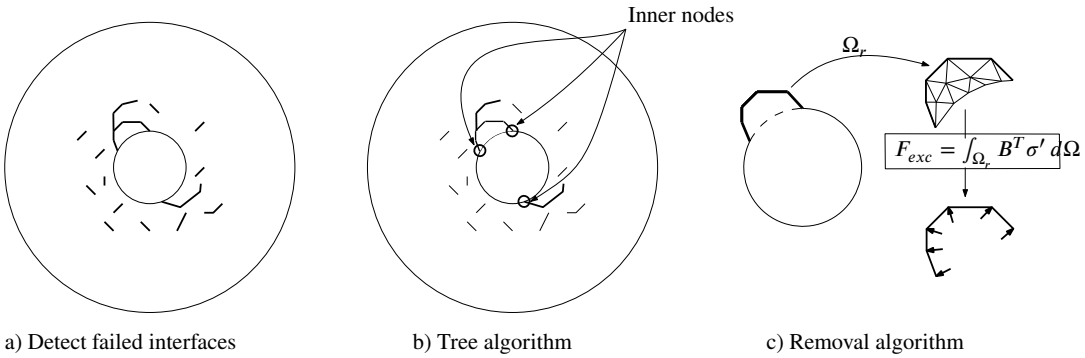


**FIGURE 19** Simplified scheme of the sand production methodology.

sand production prediction of the HCT, using the material parameters already described in Section 2.4 and depicted in Tables 2 and 3 ).

## 4.1 | Sensitivity of HCT calculation to the perforation diameter

The objective of this study is to show the capability of the model to capture the scale effect in HCT performed on perforations with different internal diameter. For this purpose, calculations of HCT test have been carried out with three different perforation radii $r_{inner} = 0.25\,\text{cm}, 0.5\,\text{cm}$ and $1.0\,\text{cm}$ (see Fig. 20 and Table 5 ). In all cases the material parameters including the material microstructure ($\varnothing_{grain} = 0.6\,\text{mm}$) were fixed and only the inner hole radius was varied.

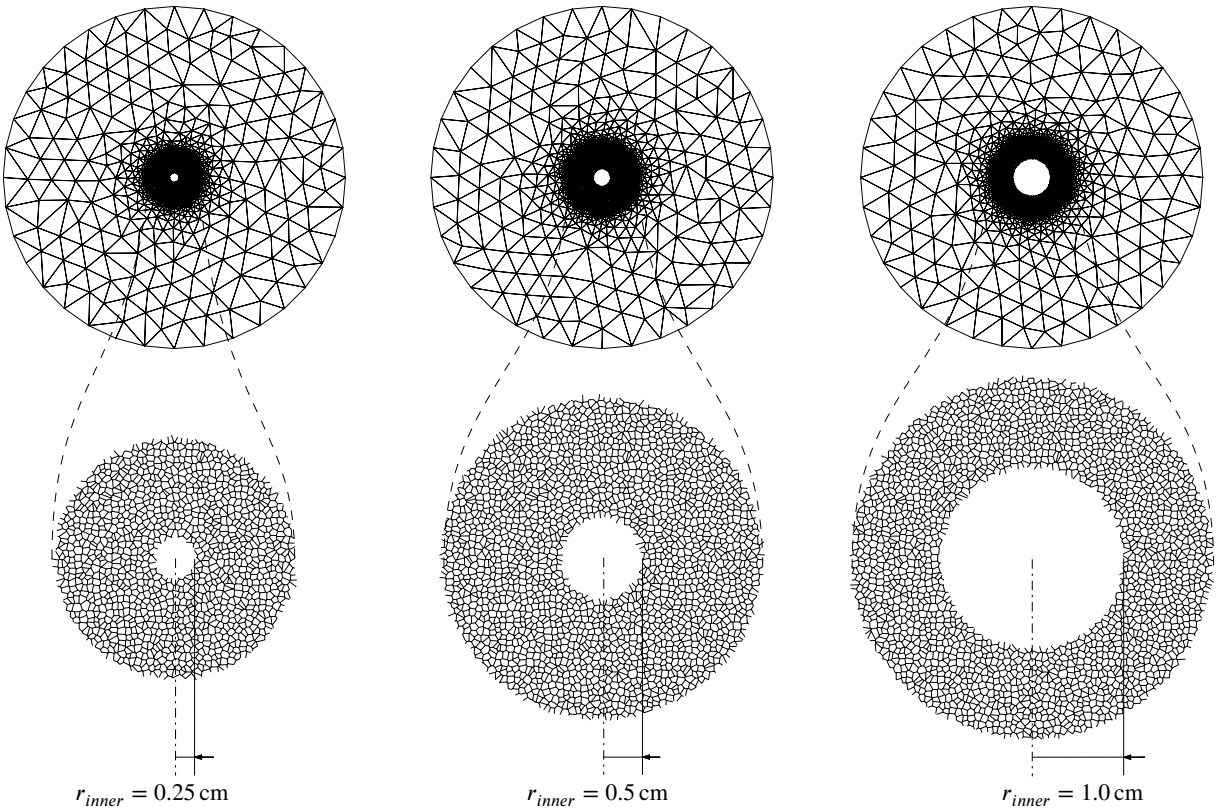


**FIGURE 20** Model geometries of internal radius sensitivity analysis. Internal radius ($r_{inner}$) from left to right: 0.25 cm, 0.5 cm and 1.0 cm. In full model (top) and detail of the discrete domain (bottom) only inter-grain interfaces are represented.

**TABLE 5** Model geometries for the internal radius sensitivity analysis.

| Geometry dimensions | Very small | Small | Common |
|---|---|---|---|
| Inner radius ($r_{inner}$) | 0.25 cm | 0.5 cm | 1.0 cm |
| Intermediate radius ($r_{outer}^{discr}$) | 1.4 cm | 1.8 cm | 2.1 cm |
| Outer radius ($r_{outer}$) | 10 cm | 10 cm | 10 cm |
| Grain diameter ($\varnothing_{grain}$) | 0.6 mm | 0.6 mm | 0.6 mm |
| **Mesh dimensions** | | | |
| n. nodes | 22 649 | 38 120 | 38 822 |
| n. continuum | 9340 | 14 767 | 15 369 |
| n. zero-thickness | 10 810 | 18 455 | 18 647 |

The obtained results are shown in Fig. 21 in terms of the accumulated sand production vs applied external compression stress. The results show clearly that the external collapse load increases as the internal radius decreases. Therefore, this limit load, called Hollow Cylinder Strength, does exhibit a clear size effect with respect to the perforation radius. Table 6 summarizes the results for the onset of sand production and the collapse pressure of the three calculations. It is noted that this result is obtained naturally from the proposed method as the material parameters have exactly the same values in the three calculations. This outcome is due to the combination of using interface elements of zero-thickness to represent cracks and the formulated constitutive law, and the way in which the degradation (softening) of the strength parameters of the interface is postulated.

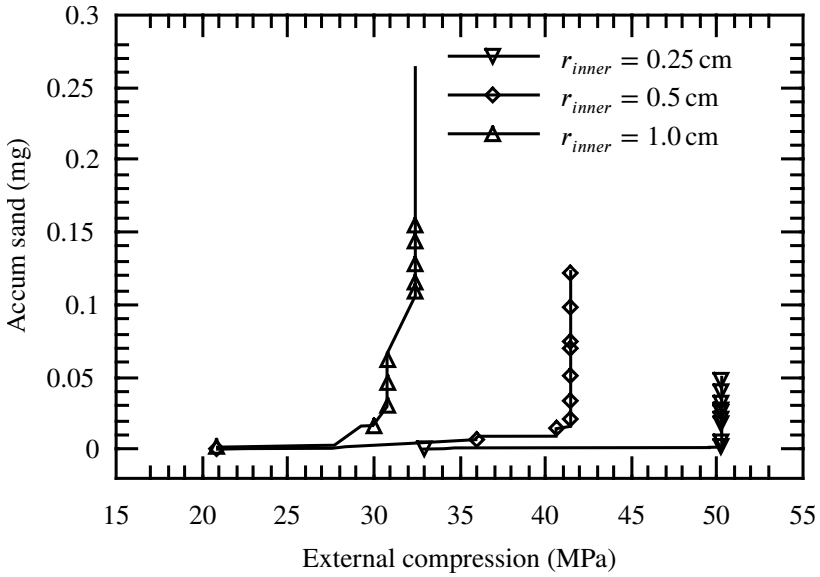


**FIGURE 21** Accumulated sand production with increasing load, for the HCT with three different perforation diameters.

As already explained in Section 2.3, the constitutive law of the interfaces uses as a history variable the dissipated fracture energy defined by the energy release rate model parameters of modes I and II, $G_f^I$ and $G_f^{IIa}$ , respectively. This implies that the energy consumed by the model to create a certain crack extension will be proportional to the area created. In contrast, classical continuum models with constitutive law with similar parameters do not have the mechanism to account properly for the energy dissipation. Remediation of this deficiency with enhanced continuum models require complex regularization techniques. In this study the model automatically exhibits size effects as a direct consequence of the correct energy dissipation per unit new crack area created[29]. Figure 22 shows the resulting geometry with the energy spent over the remaining interfaces after 50 stages of

**TABLE 6** Onset pressure and collapse pressure for different perforation diameters.

| Perforation ($r_{inner}$) | 0.25 cm | 0.5 cm | 1.0 cm |
|---|---|---|---|
| Onset pressure | 33 MPa | 21 MPa | 21 MPa |
| Collapse pressure | 50.5 MPa | 41.7 MPa | 32.7 MPa |

material removal. It can be clearly observed, from a qualitative point of view, that the damage is higher for larger perforations diameters.

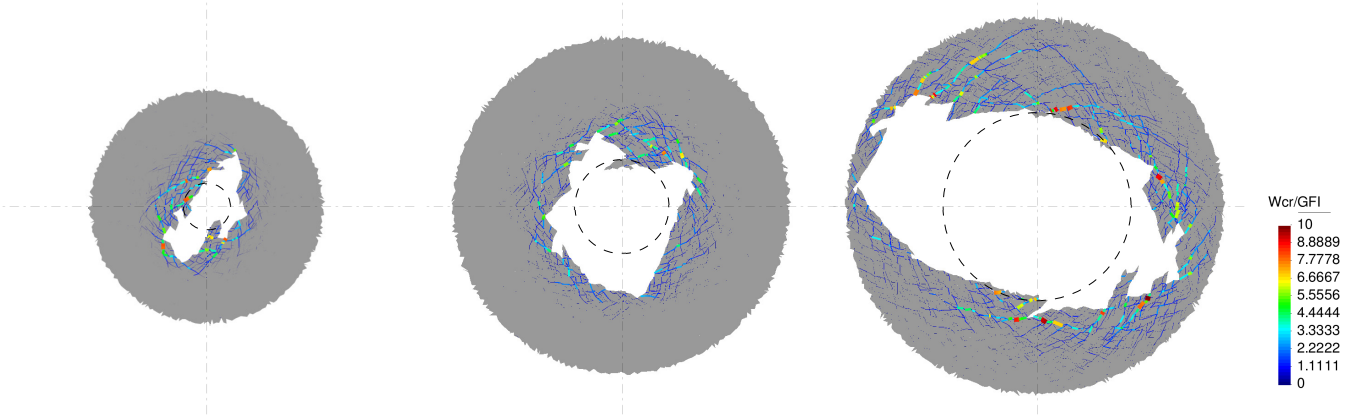


a) $r_{inner} = 0.25$ cm b) $r_{inner} = 0.5$ cm c) $r_{inner} = 1.0$ cm

**FIGURE 22** Normalized energy spent ($W^{cr}/G_f^I$) along interface elements in the HCT with three perforation diameters, after 50 stages of grain removal. Results were plotted on the deformed meshes of the discrete domain (magnification ×5).

In Fig. 23 we compared the obtained results with a simple equation which can predict the scale effect of a HCT. This equation was derived from an asymptotic analysis of a borehole failure model that is based on fracture mechanics and layer buckling theories[37,4]. According to that model an approximate solution of a Hollow Cylinder Strength (HCS) is given by

$$\mathrm{HCS} = C_1 R^{-2/5} + C_0 \tag{7}$$

where the constant $C_0$ is calibrated from the solution of a large hole found to be approximately $C_0 = 1.43 \cdot \mathrm{UCS}$, $R$ is the hole radius, and the constant $C_1$ was calibrated to match the results of one hole-size prediction, $C_1 = 41.68\,\mathrm{MPa} \cdot \mathrm{m}^{2/5}$. As we see from the comparison, the model predictions for the other two hole sizes agrees quite well with the predictions of the analytical equation both exhibiting strong scale effect.

In Fig. 24 the model predictions are compared with the experimental results performed with three different sandstones in hollow cylinder tests with different hole size[6,7]. The results of the model prediction agree well with the experimental results following the strong scale effect in the range of small perforations. The vertical axis in this plot was normalized by the UCS of each rock in order to allow comparison of the results for different sandstones. In addition, a correction factor was applied in order to refer the experimental results which were obtained with different hollow cylinder thickness to the infinite problem[4]. For the model prediction of this study no such correction is needed as the ratio of external to internal radius is near 10 which eliminates any remote boundary effect.

## 4.2 | Sensitivity to the grain size and to the microstructural parameter values

Sensitivity to intra-grain strength is evaluated with two additional simulations assuming a grain size $\varnothing_{grain} = 0.6$ mm and an internal radius $r_{inner} = 1$ cm. The first additional simulation assumes elasticity (infinite strength) for the intra-grain interfaces. This simulation could be considered as a lower bound analysis in terms of the amount of cracking, as by not allowing the grains to crack, the overall cracking will be lower at the same level of external loading. On the other hand, in terms of strength

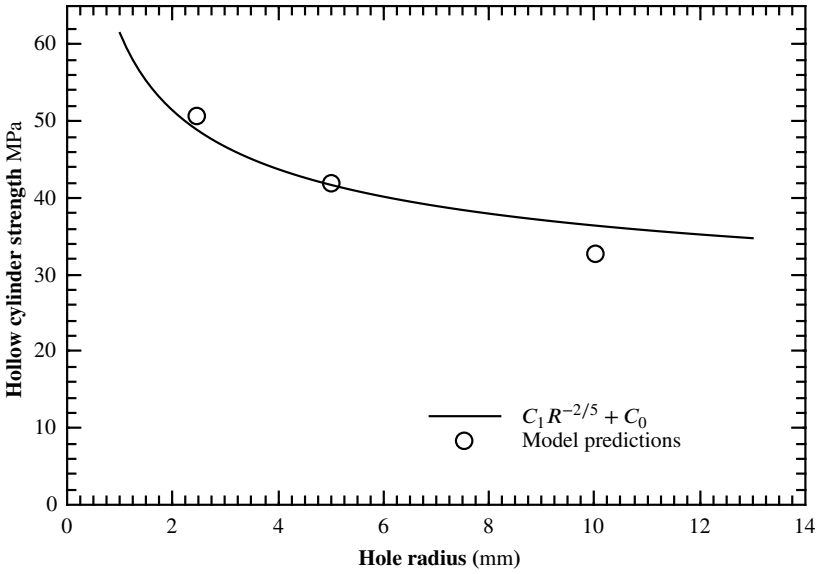


**FIGURE 23** Comparison of the model predictions and analytical solution on scale effect.

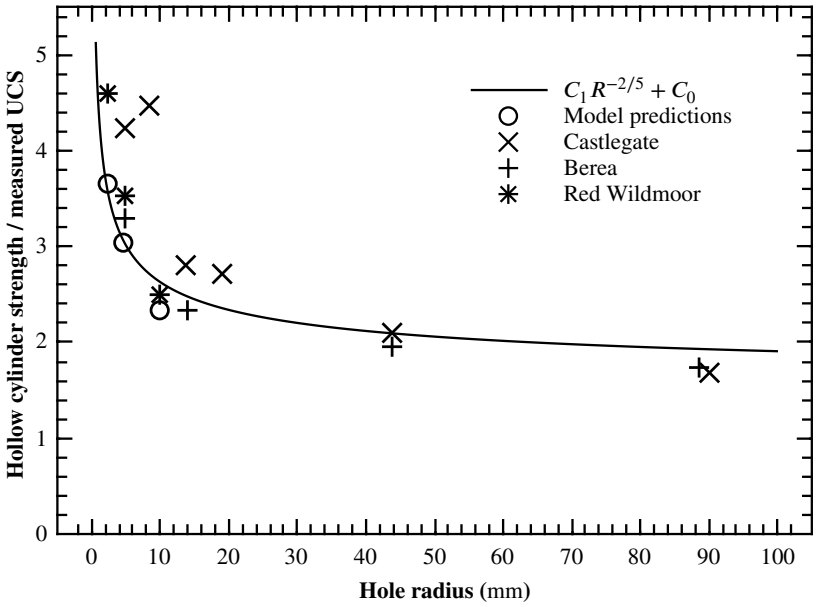


**FIGURE 24** Comparison of the model predictions with hollow cylinder experimental results performed with three different sandstones and different hole sizes[6,7].

this case corresponds to an upper bound, since higher external load will be needed to overcome the additional friction due to the microstructural geometry, as cracks have to develop around grains resulting in much higher shear loads. The second case assumes the same strength for both intra-grain and inter-grain interfaces. This case could be considered as an upper limit from a production point of view, and a lower limit from the viewpoint of the overall strength.

The results shown in Fig. 25 exhibit a clear effect of intra-grain strength on sand production. Sand production is triggered at lowest load of 20 MPa in the case of same strength in all interfaces and about 50% higher (30 MPa) for the case of double strength in intra-granular interfaces. The elastic case reaches an external load up to 95 MPa without showing evidences of collapsing and with a small rate of sand accumulation. The last simulation ended unsuccessfully due to numerical problems, probably related to extreme brittle behaviour. Figure 26 shows the energy dissipated along remaining interfaces at the end of each test. It is

interesting to observe how the internal strength of the grains may affect the crack pattern. The results show that as the intra-grain strength decreases, the tendency to localization leading to larger breakout failures increases.

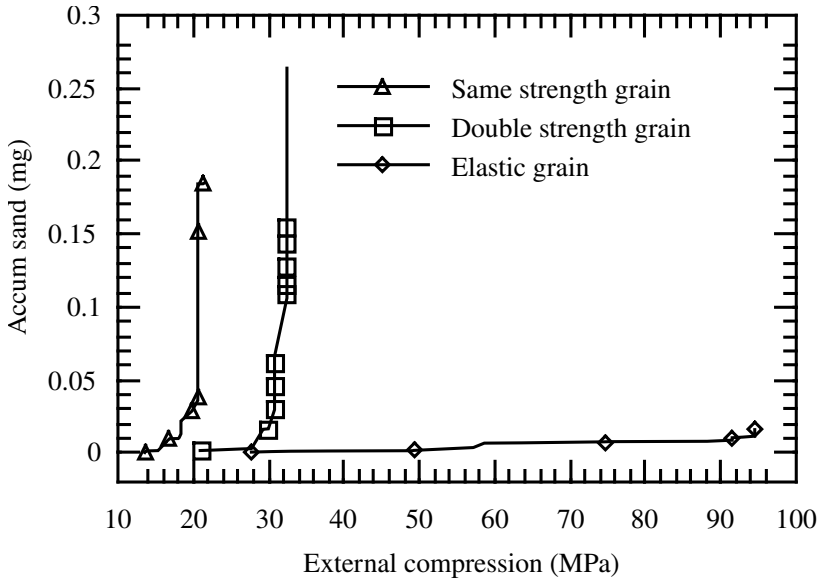


**FIGURE 25** Curves of accumulated sand production for various assumptions of inter-granular strength.

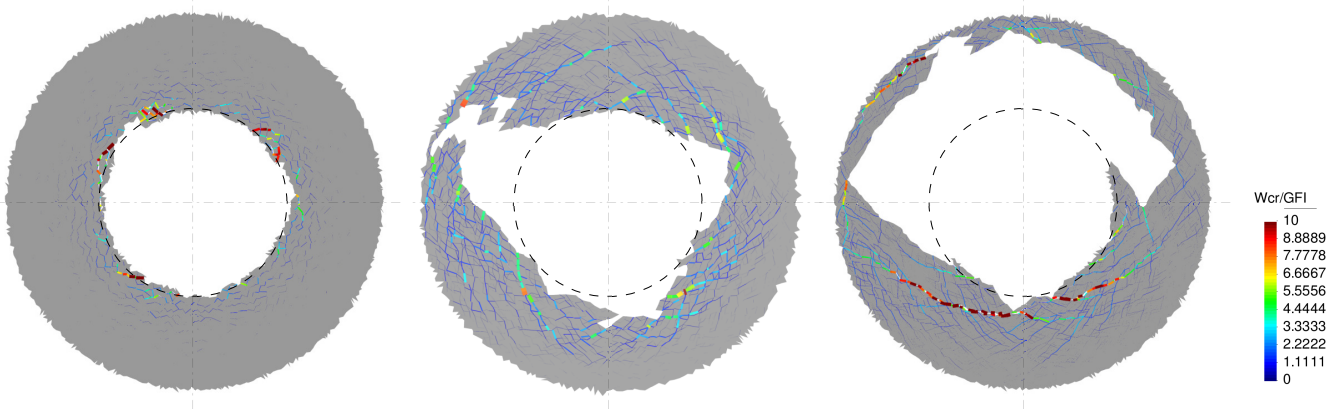


a) Intra-grain = elastic (no fracture) b) Intra-grain = 2×Inter grain c) Intra-grain = Inter grain

**FIGURE 26** Normalized energy spent ($W^{cr}/G_f^I$) along remaining interfaces for different values of intra-grain strength at the end of test: a) Elastic interface, no failure of grain is possible, b) The resistance of intra-grains is greater (cohesion and tensile strength double), and c) Same strength between intra and inter grain interfaces. Results plotted on deformed meshes of discrete domain (magnification ×5).

The sensitivity to grain diameter was investigated by analysing three cases with grain diameter of 0.6 mm, 0.9 mm and 1.2 mm with same strength for all interfaces (intra or inter grain) (Fig. 27 ). The results depicted in Fig. 28 do not show a clear effect of the grain diameter on sand production which could be somehow expected. Figure 29 shows the energy dissipated along the remaining interfaces at the end of each test. We note that the results of the influence of the grain size on sanding will depend also on the assumed intra-granural strength. Greater dependence on the grain size is expected in the case of high intra-granural strength as in this case the cracking will follow the grain boundaries resulting in a more tortuous path.

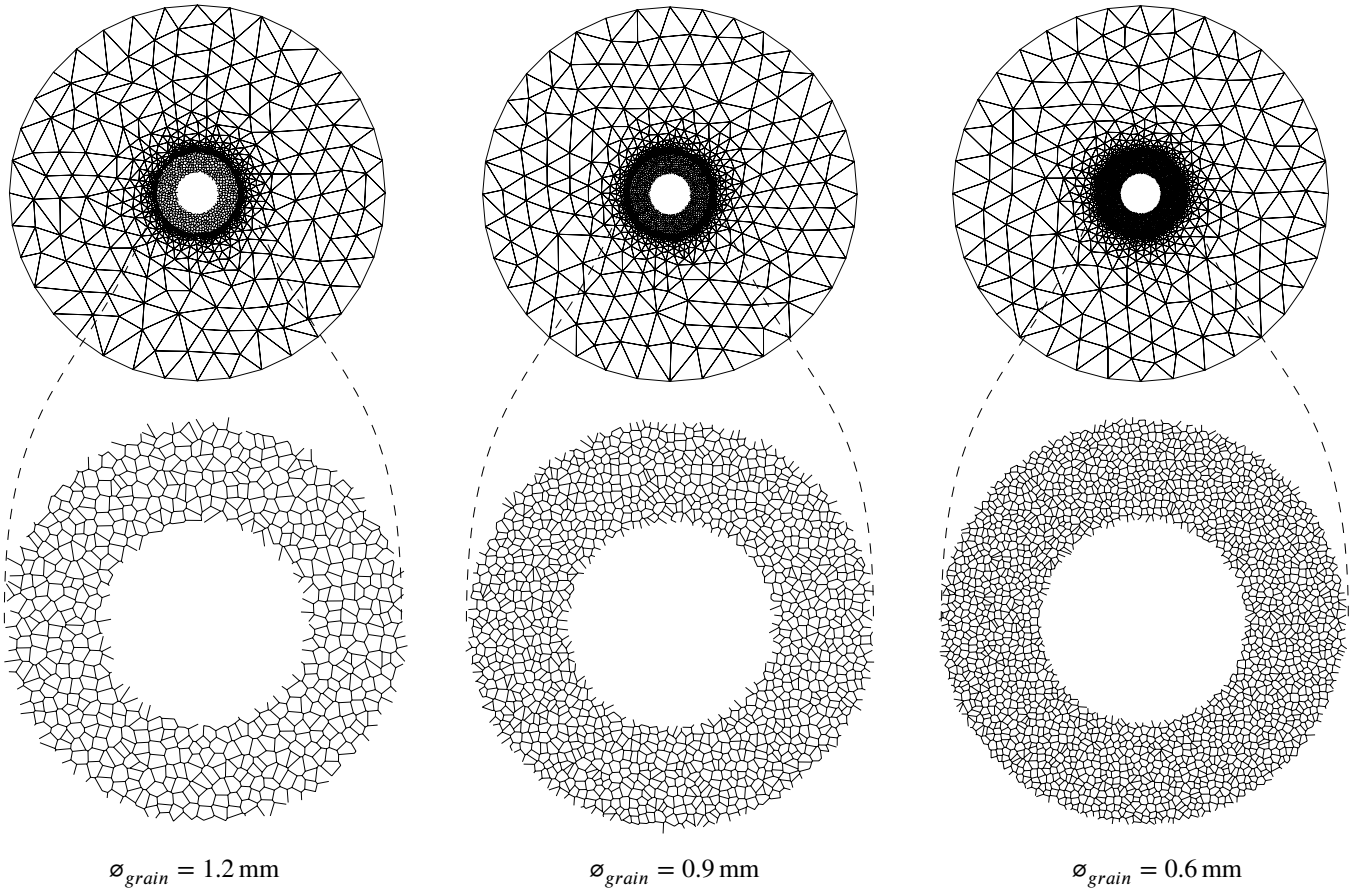


**FIGURE 27** Model geometries of grain size sensitivity analysis, in full model(top) and detail of the discrete domain (bottom). Only the inter-grain interfaces are represented.

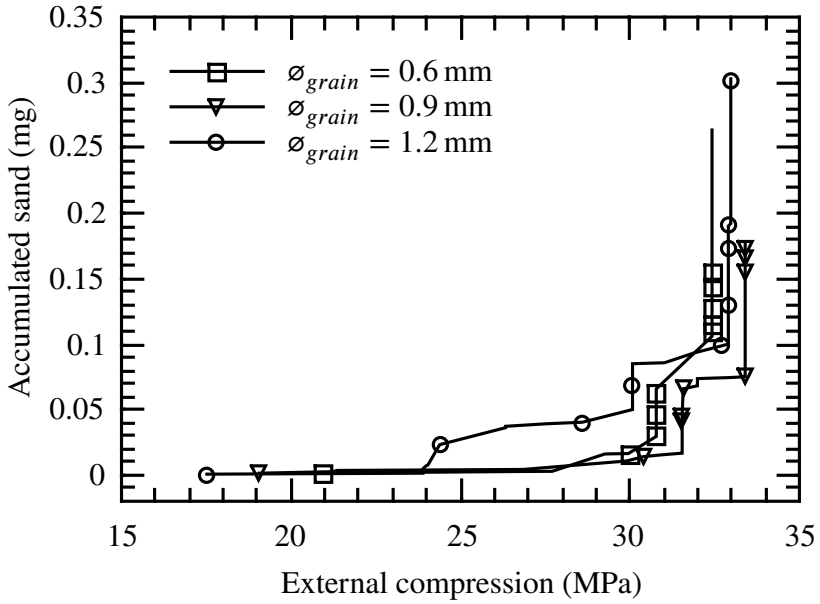


**FIGURE 28** Curves of accumulated sand production for different grain diameters.

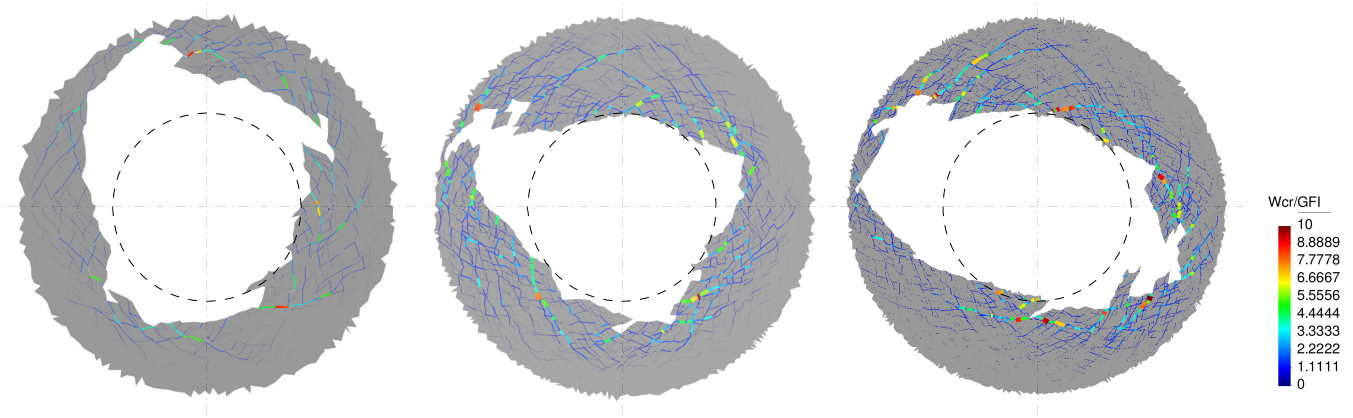


a) $\varnothing_{grain} = 1.2\,\text{mm}$ b) $\varnothing_{grain} = 0.9\,\text{mm}$ c) $\varnothing_{grain} = 0.6\,\text{mm}$

**FIGURE 29** Normalized energy spent ($W^{cr}/G_f^I$) along remaining interfaces for different values of grain diameter at the end of each test. The results are plotted on deformed meshes of the discrete domain (magnification ×5).

## 5 | CONCLUSIONS

We have presented a micromechanical approach based on zero thickness interface finite elements for modelling advanced deformation, localization and cracking states of cemented granular materials, such as sandstones. The proposed methodology is capable of reproducing the complex behaviour of inter-granular and intra-granular cracking and fracturing using only a few physical parameters derived at micro and meso scales. The model is calibrated at the macro-scale by reproducing the typical behaviour of compression element tests. The model exhibits clear transition from brittle dilatant to ductile compactant behaviour with increasing confining stress. Furthermore, the inclination of the shear/cracking bands agree well with the theoretical predictions. The methodology is implemented for sand prediction analysis based on the simulation of 2D micromechanical models of hollow cylinder cross-sections. The increase in computational resources due to discretization of the grain area is compensated by modelling the remote area with continuum finite elements. We presented sensitive analysis for the main model input and parameters such as perforation size, grain diameter and inter-granular to intra-granular strength relations. The obtained results are compared well with published analytical and experimental data from hollow cylinder tests performed on different sandstones covering a wide range of perforation sizes.

## ACKNOWLEDGMENTS

The work was partially supported by research grants BIA2016-76543-R from MEC (Madrid), which includes FEDER funds from the European Union, and 2017SGR-1153 from Generalitat de Catalunya (Barcelona). The first author would like to thank the MEC (Madrid) for his FPU doctoral fellowship.

## References


1. Fjaer E., Holt R. M., Horsrud P., Raaen A. M., Risnes R.. *Petroleum related rock mechanics*. Elsevier; 2nd ed. 2008.

2. Han G.. Rock Stability under Different Fluid Flow Conditions. PhD dissertation. Departament of Chemical Engineering, University of Waterloo. Canada. 2003.

3. Dusseault M.B., Santarelli F.J. A conceptual model for massive solids production in poorly-consolidated sandstones. *Rock at Great Depth. Proceedings ISRM/SPE.* 1989;2:789-797.

4. Papanastasiou P., Thiercelin M.. Modeling Borehole and Perforation Collapse with the Capability of Predicting the Scale Effect. *International Journal of Geomechanics.* 2011;11(4):286-293.

5. Haimson B. C., Herrick C.. Borehole breakouts and in situ stress.. In: Rowley J. C., ed. *Proc. Drilling Symp*, ASME; 1989.

6. Tronvoll J., Papamichos E., Kessler N.. Perforation cavity stability: Investigation of failure mechanisms.. In: editor , ed. *Proc. Symp. Hard Soils Soft Rocks*, :1687–1693; 1993.

7. Papamichos E., Hoek P. J. Van. Size dependency of Castlegate and Berea sandstone hollow-cylinder strength on the basis of bifurcation theory. In: editor , ed. *The 35th U.S. Symposium on Rock Mechanics (USRMS), Reno, Nevada*, ARMA-95-0301:301-306. Balkema; 1995.

8. Papanastasiou P., Vardoulakis I.. Bifurcation analysis of deep boreholes: II. Scale effect. *International Journal for Numerical and Analytical Methods in Geomechanics.* 1989;13(2):183-198.

9. Papanastasiou P., Vardoulakis I.. Numerical treatment of progressive localization in relation to borehole stability. *International Journal for Numerical and Analytical Methods in Geomechanics.* 1992;16(6):389-424.

10. Papamichos E.. Borehole failure analysis in a sandstone under anisotropic stresses. *International Journal for Numerical and Analytical Methods in Geomechanics.* 2010;34(6):581-603.

11. Zervos A., Papanastasiou P., Vardoulakis I.. Modelling of localisation and scale effect in thick-walled cylinders with gradient elastoplasticity. *International Journal of Solids and Structures.* 2001;38(30-31):5081 - 5095.

12. Papanastasiou P., Zervos A.. Wellbore Stability Analysis: From Linear Elasticity to Postbifurcation Modeling. *International Journal of Geomechanics.* 2004;4(1):2-12.

13. Vardoulakis I., Stavropoulou M., Papanastasiou P.. Hydromechanical aspects of sand production problem. *Transport in Porous Media.* 1996;22:225–244.

14. Stavropoulou M., Papanastasiou P., Vardoulakis I.. Coupled well bore erosion and stability analysis. *International Journal for Numerical and Analytical Methods in Geomechanics.* 1998;22:749–769.

15. Papamichos E., Stavropoulou M.. An erosion-mechanical model for sand production rate prediction. *International Journal of Rock Mechanics and Mining Sciences.* 1998;35(4):531 - 532.

16. Papamichos E., Vardoulakis I., Tronvoll J., Skjaerstein A.. Volumetric sand production model and experiment. *International Journal for Numerical and Analytical Methods in Geomechanics.* 2001;25(8):789–808.

17. Gravanis E., Sarris E., Papanastasiou P.. Hydro-mechanical erosion models for sand production. *International Journal for Numerical and Analytical Methods in Geomechanics.* 2015;39(18):2017-2036.

18. Jensen R.P., Preece D.S., Cook B.K., Williams J.R.. Modeling sand production with darcy coupled with discrete elements. In: al. Desai, ed. *Comp. Meth. And Adv. In Geomech*, Rotterdam: Balkema 2001 (pp. 819–822).

19. Li L., Papamichos E., Cerasi P.. Investigation of sand production mechanisms using DEM with fluid flow. In: Cotthem A., Charlier R., Thimus JF., Tshibangu JP., eds. *Eurock 2006: Multiphysics Coupling and Long Term Behaviour in Rock Mechanics*, :241–247International Society for Rock Mechanics; Taylor & Francis; 2006.

20. Carol I., López C.M., Roa O.. Micromechanical analysis of quasi-brittle materials using fracture-based interface elements. *International Journal for Numerical Methods in Engineering.* 2001;52:193–215.

21. Garolera D., López C.M., Carol I., Papanastasiou P.. Micromechanical Analysis of the Rock Sanding Problem. *Journal of the Mechanical Behavior of Materials.* 2005;16(1-2):45-54.

22. Garolera D.. Zero-thickness interface elements in petroleum geomechanics: sand production and hydraulic fracture. PhD thesis. Barcelona School of Civil Engineering, Universitat Politècnica de Catalunya. 2017.

23. López C.M., Carol I., Aguado A.. Meso-structural study of concrete fracture using interface elements. I: numerical model and tensile behavior. *Materials and Structures.* 2008;41(3):583–599.

24. Caballero A., Carol I., López C.M.. A meso-level approach to the 3D numerical analysis of cracking and fracture of concrete materials. *Fatigue and Fracture of Engineering Materials and Structures.* 2006;29(12):979–991.

25. Wittmann F.H.. Structure of concrete with respect to crack formation. In: Wittmann F.H., ed. *Fracture mechanics of concrete*, Elsevier 1983 (pp. 43–74).

26. López C. M.. Análisis microestructural de la fractura del hormigón utilizando elementos finitos tipo junta. Aplicación a diferentes hormigones. PhD thesis. Barcelona School of Civil Engineering, Universitat Politècnica de Catalunya. 1999.

27. Stankowski T.. Numerical simulation of progressive failure in particle composites. PhD thesis. University of Colorado, USA. 1990.

28. Vonk R.. Softening of concrete loaded in compression. PhD thesis. TU Eindhoven, The Netherlands. 1992.

29. Bažant Z.P., Planas J.. *Fracture and Size Effect in Concrete and Other Quasibrittle Materials*. CRC Press; 1998.

30. Carol I., Prat P., López C.M.. Normal/shear cracking model: application to discrete crack analysis. *Journal of engineering mechanics.* 1997;123(8):765–773.

31. Caballero A., Willam K.J., Carol I.. Consistent tangent formulation for 3D interface modeling of cracking/fracture in quasi-brittle materials. *Computer Methods in Applied Mechanics and Engineering.* 2008;197(33–40):2804 - 2822.

32. Carol I., Prat P.. A statically constrained microplane model for the smeared analysis of concrete cracking. In: Bićanić N., Mang H., eds. *Computer-Aided Analysis and Design of Concrete Structures*, :919-930; 1990.

33. Papamichos E., Tronvoll J., Vardoulakis I., et al. Constitutive testing of Red Wildmoor sandstone. *Mechanics of Cohesive-frictional Materials.* 2000;5(1):1-40.

34. Vliet Marcel R.A., Mier Jan G.M.. Experimental investigation of size effect in concrete and sandstone under uniaxial tension. *Engineering Fracture Mechanics.* 2000;65(2):165 - 188.

35. Prat P., Gens A., Carol I., Ledesma A., Gili J.A.. DRAC: A computer software for the analysis of rock mechanics problems. In: Liu H., ed. *Application of Computer Methods in Rock Mechanics in Rock Mechanics.*, :1361-1368. Shaanxi Science and Technology Press; 1993.

36. Cuss R.J., Rutter E.H., Holloway R.F.. Experimental observations of the mechanics of borehole failure in porous sandstone. *International Journal of Rock Mechanics and Mining Sciences.* 2003;40(5):747 - 761.

37. Bažant Z.P., Lin F., Lippmann H.. Fracture energy release and size effect in borehole breakout. *International Journal for Numerical and Analytical Methods in Geomechanics.* 1993;17(1):1-14.